

16 **Abstract**

17 Taking the full complexity of subduction zones into account is important for
 18 realistic modelling and hazard assessment of subduction zone seismicity and associated
 19 tsunamis. Studying seismicity requires numerical methods that span a large range
 20 of spatial and temporal scales. We present the first coupled framework that resolves
 21 subduction dynamics over millions of years and earthquake dynamics down to fractions
 22 of a second. Using a two-dimensional geodynamic seismic cycle (SC) method, we
 23 model 4 million years of subduction followed by cycles of spontaneous megathrust
 24 events. At the initiation of one such SC event, we export the self-consistent fault
 25 and surface geometry, fault stress and strength, and heterogeneous material properties
 26 to a dynamic rupture (DR) model. Coupling leads to spontaneous dynamic rupture
 27 nucleation, propagation and arrest with the same spatial characteristics as in the SC
 28 model. It also results in a similar material-dependent stress drop, although dynamic
 29 slip is significantly larger. The DR event shows a high degree of complexity, featuring
 30 various rupture styles and speeds, precursory phases, and fault reactivation. Compared
 31 to a coupled model with homogeneous material properties, accounting for realistic
 32 lithological contrasts doubles the amount of maximum slip, introduces local pulse-
 33 like rupture episodes, and relocates the peak slip from near the downdip limit of
 34 the seismogenic zone to the updip limit. When an SC splay fault is included in the
 35 DR model, the rupture prefers the splay over the shallow megathrust, although wave
 36 reflections do activate the megathrust afterwards.

37 **1 Introduction**

38 Throughout the past decades, enigmatic observations of subduction zone earth-
 39 quakes have repeatedly given rise to new insights. For example, large slip occurring
 40 up to the trench during the 2011 M_w 9.0 Tōhoku-Oki earthquake demonstrated how
 41 poorly the occurrence of slip in shallow, presumably velocity-strengthening regions is
 42 understood to date (Fujiwara et al., 2011; Lay et al., 2011).

43 Understanding the seismic characteristics along megathrusts from the trench to
 44 the down-dip limit of the seismogenic zone is crucial for improving the assessment
 45 of seismic — and the associated tsunami — hazards. However, the physics governing
 46 subduction zone seismicity occurs on a wide range of temporal scales. Tectonic stresses
 47 build up over millions of years and are episodically released during earthquakes, which
 48 initiate, propagate, and stop on time scales smaller than seconds. Capturing the
 49 relevant physics across these time scales is computationally and numerically challenging
 50 and currently not yet feasible within a single modelling framework.

51 Geodynamic modelling usually tackles large scale, long-term problems, such as
 52 subduction zone evolution on a lithospheric or global scale over millions of years (see
 53 Billen, 2008; Gerya, 2011, for an overview). Such models provide insight into the
 54 formation and geometry of megathrust faults and the corresponding state of stress
 55 (Billen et al., 2003; Goes et al., 2017). However, most geodynamic models do not
 56 include elastic rheologies (Patočka et al., 2017) and resolve the physical processes on
 57 time scales on the order of thousands of years at most. These restrictions render them
 58 unsuitable for studying seismicity or earthquake rupture dynamics.

59 In contrast, seismic cycle models of the megathrust focus on smaller time scales
 60 spanning thousands of years down to coseismic time scales smaller than seconds (e.g.,
 61 Rice, 1993; Ben-Zion & Rice, 1997; Lapusta et al., 2000; Liu & Rice, 2007; Langer
 62 et al., 2010; Kaneko et al., 2011). By modelling both long-term loading of predefined
 63 faults and spontaneous rupture across these faults, seismic cycle models can provide
 64 insight into interseismic stress build-up, coseismic rupture processes, and postseismic
 65 relaxation. However, the majority of seismic cycle models use quasi-static or quasi-

66 dynamic approximations which do not account for the stresses mediated by the emitted
67 seismic waves. Notable fully dynamic exceptions by, for example, Lapusta et al. (2000)
68 and Kaneko et al. (2011), are algorithmically and computationally challenging.

69 Seismic cycle models are commonly limited to predefined faults, which are of-
70 ten simplified to planar geometries. These restrictions may result from the employed
71 numerical scheme related to the spatial discretisation or the available computational
72 resources. Furthermore, widely applied seismic cycle methods may inherently only
73 account for homogeneous elastic media (Lapusta et al., 2000). While providing fun-
74 damental insight into the mechanics of the earthquake cycle, observations indicate
75 multi-fault geometries and complex lithologies (e.g., Kodaira et al., 2002), which can-
76 not yet be accounted for in state-of-the-art seismic cycle models.

77 Dynamic rupture models are designed to study the dynamics of earthquakes at
78 coseismic time scales. Dynamic rupture modelling has been pioneered by e.g., An-
79 drews (1973); Das (1980); Day (1982); Madariaga et al. (1998); Oglesby et al. (1998);
80 Ampuero et al. (2002); Dalguer and Day (2007). Such models provide physically self-
81 consistent earthquake source descriptions by modelling spontaneous frictional failure
82 across a predefined fault coupled to seismic wave propagation. By using modern numer-
83 ical methods and hardware specific software optimisation, dynamic rupture simulations
84 can reach high spatial and temporal resolution of increasingly complex geometrical and
85 physical modelling components (Wollherr, Gabriel, & Mai, 2019; Ulrich et al., 2018).
86 In comparison to the aforementioned approaches, such models fully incorporate inertia
87 effects as well as the non-linear interaction of seismic waves and fault mechanics
88 governed by friction.

89 However, the dynamic rupture community faces challenges in constraining the
90 initial conditions governing fault stresses and strengths. These are integral ingredients
91 of the dynamic rupture, as they govern the rupture propagation style (e.g., crack-
92 versus pulse-like dynamics and sub- versus supershear rupture speeds), transfers (e.g.,
93 dynamic triggering potential), and earthquake arrest (e.g., Kame et al., 2003; Bai &
94 Ampuero, 2017).

95 Another important open question is how to constrain the rupture nucleation
96 process and hypocenter in a physically consistent manner. Dynamic rupture models
97 typically use artificially enforced slip initiation by, e.g., locally reducing the static
98 friction coefficient (Harris, 2004; Harris et al., 2009, 2011, 2018). However, the ensuing
99 rupture is highly sensitive to the chosen nucleation approach and its computational
100 resolution in time and space (Bizzarri, 2010; Gabriel et al., 2012, 2013; Galis et al.,
101 2014). In addition, the location of the hypocenter may be chosen ad-hoc without a
102 strong physical basis. Studying earthquake nucleation beyond ad-hoc approaches will
103 further our understanding of the interaction of megathrust earthquakes, foreshocks
104 and aseismic processes.

105 Ideally, the initial states of stress and fault strength are self-consistent and con-
106 sistent with the geometry and rheology of the subsurface and fault networks. However,
107 due to a lack of constraints, especially on the amplitude of fault-local tractions, fault
108 normal and shear tractions are commonly prescribed as constant or linearly increas-
109 ing with depth in dynamic rupture models (Kozdon et al., 2013; Kozdon & Dunham,
110 2013; Galvez et al., 2014, 2018). Direct measurements of on-fault stresses are diffi-
111 cult to obtain, but inferences from nearby borehole measurements and observations
112 of stress orientations and rotations do provide insight on the shear and normal trac-
113 tions acting on megathrusts (Chang et al., 2010; Hardebeck, 2012; Fulton et al., 2013;
114 Hardebeck, 2015). Dynamic rupture models have successfully incorporated such ob-
115 servations by projecting the inferred regional stress information onto spatially complex
116 fault geometries (Aochi & Fukuyama, 2002; Aagaard et al., 2004; Gabriel & Pelties,
117 2014; Heinecke et al., 2014; Uphoff et al., 2017; Bauer et al., 2017; Madden et al.,

118 2018; Ulrich et al., 2018; Wollherr et al., 2018). However, it is difficult to account for
119 variable loading on different fault segments, local lithological heterogeneities, stress
120 and fault roughness, stress interactions between faults and their surroundings, and the
121 different stages of faults within their seismic cycle (Herrendörfer, 2018; Romanet et
122 al., 2018).

123 The in situ fault strength is equally hard to constrain. Most studies focus on
124 experimentally constraining the frictional behaviour of rocks at coseismic slip velocities
125 (Dieterich, 1979; Ruina, 1983; Di Toro et al., 2011; den Hartog et al., 2012). Drilling
126 experiments and heat flow measurements provide to-scale insight on the frictional
127 strength of megathrusts (Fulton et al., 2013). Observational studies indirectly infer
128 the distribution of the pore fluid pressure ratio in subduction zones (Seno, 2009).
129 Various modelling efforts are also aimed at understanding the role of fluids on the
130 strength of the megathrust (Angiboust et al., 2012; Petrini et al., 2017). Despite these
131 advances, a major challenge is the large scaling difference between natural subduction
132 zones, small-scale laboratory experiments, and localised, isolated field measurements.

133 Due to their locations, the exact fault geometry of subduction zones is often
134 unknown. Splay faults are seaward verging crustal faults that splay away from the main
135 subduction megathrust interface at shallow depth. They may rupture in addition to or
136 instead of parts of the megathrust. It has been suggested that these splay faults play
137 an important role during tsunamigenesis, because they could potentially accommodate
138 large vertical displacements (Fukao, 1979). Therefore, several dynamic rupture studies
139 have investigated fault branching and splay fault activation, mostly using simplified
140 geometries (Wendt et al., 2009; Tamura & Ide, 2011; DeDontney & Rice, 2012; Li et
141 al., 2014; Madden et al., 2017; Uphoff et al., 2017). Choosing appropriate stress and
142 strength for both the megathrust and the splay fault has been shown to crucially affect
143 branching and dynamic triggering (DeDontney et al., 2012; DeDontney & Hubbard,
144 2012).

145 “Seismo-thermo-mechanical” models provide insight into complex subduction
146 zone features, such as the role of rheology, temperature, and fault geometry and evo-
147 lution, including spontaneously evolving splay faults (e.g., van Dinther et al., 2014;
148 Herrendörfer et al., 2015; Corbi et al., 2017; Dal Zilio et al., 2018, 2019; Preuss et al.,
149 2019). These models bridge the time scales of traditional geodynamic and seismic cycle
150 models, as initiated by van Dinther, Gerya, Dalguer, Corbi, et al. (2013); van Dinther,
151 Gerya, Dalguer, Mai, et al. (2013). The therein developed two-dimensional model
152 includes the long-term dynamics of subduction, as well as short-term frictional slip
153 transients. However, these models cannot resolve the inertial dynamics of slip events
154 due to numerical restrictions. The minimum resolution is 5 years in time and 500 m
155 in space. The limitations in spatio-temporal resolution were recently overcome for a
156 strike-slip setup with the seismo-thermo-mechanical rate-and-state friction method-
157 ology (Herrendörfer et al., 2018). However, applying this methodology to the more
158 challenging setting of a subduction zone does not yet result in accurately crossing all
159 time scales. In a thermo-mechanically evolving subduction zone, tectonic loading is
160 limited to hundreds of thousands of years, instead of millions of years. Besides that,
161 slow slip events have a maximum slip rate on the order of 10^{-7} m/s (Herrendörfer,
162 2018). Sobolev and Muldashev (2017) model time scales down to minutes to resolve
163 postseismic processes in addition to subduction evolution. Nevertheless, the challenge
164 of fully resolving the subduction evolution in combination with rupture dynamics on
165 coseismic time scales remains.

166 To overcome the limitations of each of these approaches, the hereafter presented
167 coupling approach fully resolves the tectonic, seismic cycle (excluding the postseismic
168 phase), and dynamic rupture time scales for the first time by linking a transient slip
169 event of a geodynamic seismic cycle (SC) model to a dynamic rupture (DR) model. By
170 adapting the full outcome of the SC model into initial conditions for the DR model in a

171 physically consistent manner, we provide geometries of the fault and its surroundings,
 172 material properties, and fault stresses and strength. This enables us to study the
 173 complex mechanics of subduction zones and megathrust earthquakes in a physically
 174 consistent manner.

175 The work presented here is structured as follows. First, we summarise the SC
 176 and DR modelling approaches and their respective assumptions in Secs. 2 and 3.
 177 We then describe how we couple the material properties, stresses, geometry and
 178 strength conditions of a representative SC event to the DR model in Sec. 4, specifically
 179 in light of the different set of equations and assumptions both approaches use. We
 180 discuss the resulting state of stress from the long-term subduction evolution in Sec. 5.1
 181 and compare the geodynamic (Sec. 5.2) and dynamic rupture (Sec. 5.3) events in
 182 Sec. 5.4. To assess the effect of the heterogeneous, temperature-dependent material
 183 properties from the SC model on the dynamic rupture, we conduct a series of models
 184 with increasing material complexity in Sec. 5.5. In addition to a single megathrust
 185 rupture, we investigate the coseismic rupture dynamics along an additional splay fault
 186 based on the fault structures visible in the SC model (Sec. 5.6). To ensure that the
 187 coupling method is robust, we test the effect of the two main assumptions we made
 188 in Sec. 6.1: an idealised Poisson’s ratio governing seismic wave propagation in the
 189 DR model (Sec. 6.1.1) and a linear-slip weakening approximation in the DR model of
 190 the rate-weakening friction used in the SC model (Sec. 6.1.2). In Sec. 6.2, we discuss
 191 several possible future lines of work that could address the current limitations of our
 192 approach. We summarise our most important findings in Sec. 7.

193 2 Geodynamic seismic cycle model

194 We use the seismo-thermo-mechanical (STM) version of the two-dimensional,
 195 visco-elasto-plastic, continuum I2ELVIS code to solve the long-term dynamics of sub-
 196 duction zone evolution and the subsequent seismic cycle (Gerya & Yuen, 2007; van
 197 Dinther, Gerya, Dalguer, Corbi, et al., 2013; van Dinther, Gerya, Dalguer, Mai, et al.,
 198 2013; van Dinther et al., 2014). First, we briefly describe the governing equations,
 199 rheology, failure criterion, and friction formulation. We then describe the model setup
 200 in Sec. 2.4. A full description of the methods can be found in Gerya and Yuen (2007)
 201 and van Dinther, Gerya, Dalguer, Mai, et al. (2013).

202 2.1 Governing equations

203 We solve the following set of conservation equations in a two-dimensional Carte-
 204 sian coordinate system, derived from the principles of conservation of mass (1), mo-
 205 mentum (2), and energy (3):

$$\nabla \cdot \mathbf{v} = 0, \quad (1)$$

$$\rho \frac{D\mathbf{v}}{Dt} = \nabla \cdot \boldsymbol{\sigma}' - \nabla P + \rho \mathbf{g}, \quad (2)$$

$$\rho C_p \left(\frac{DT}{Dt} \right) = -\nabla \mathbf{q} + H_a + H_s + H_r. \quad (3)$$

206 All symbols and terms used in these and the following equations are described in
 207 Table 1. The continuity equation (1) assumes an incompressible medium, i.e., Poisson’s
 208 ratio $\nu = 0.5$. This is valid when pressure and temperature changes are small and
 209 therefore only minimally impact the volume of the material. The energy equation (3)
 210 describes conductive ($\nabla \mathbf{q}$) and advective heat transport (within the material derivative

Table 1. Nomenclature

Symbol	Parameter	Unit
Δx	Grid size	m
$\dot{\epsilon}_{e,v,p}$	(Elastic, viscous, plastic) Strain rate	s^{-1}
$\dot{\epsilon}_{vp,II}$	Second invariant of the visco-plastic strain rate	s^{-1}
η, η_0	Viscosity, reference viscosity equal to $1/A_d$	Pa s
η_{vp}	Effective visco-plastic viscosity	Pa s
λ	Pore fluid pressure ratio P_f/P	-
λ_1	First Lamé parameter	Pa
$\mu_{(eff)}^{sc,dr}$	(Effective) Friction coefficient (sc,dr)	-
$\mu_d^{sc,dr}$	Dynamic friction coefficient (sc,dr)	-
$\mu_s^{sc,dr}$	Static friction coefficient (sc,dr)	-
ν	Poisson's ratio	-
ρ, ρ_0	Density, reference density	$kg\ m^{-3}$
σ'_{II}	Second invariant of the deviatoric stress tensor	Pa
$\boldsymbol{\sigma}, \boldsymbol{\sigma}'$	Stress tensor, deviatoric stress tensor	Pa
σ_n	Normal stress	Pa
$\sigma_{yield}^{sc,dr}$	Yield stress (sc,dr)	Pa
$\sigma_{sliding}^{dr}$	DR sliding stress	Pa
τ	Shear stress	Pa
χ	Plastic multiplier	s^{-1}
A_D	Pre-exponential factor	$Pa^{-n}\ s^{-1}$
C	Cohesion	Pa
C_p	Isobaric heat capacity	$J\ kg^{-1}\ K^{-1}$
d	Slip	m
D_c	Characteristic slip distance	m
E_a	Activation energy	$J\ mol^{-1}$
f_{max}	Maximum resolved frequency	s^{-1}
F	Visco-elasticity factor	-
g	Gravity acceleration	$m\ s^{-2}$
G	Shear modulus	Pa
$G_{plastic}$	Plastic flow potential	Pa
H_a, H_r, H_s	Adiabatic, radioactive and shear heat production	$W\ m^{-3}$
n	Stress exponent	-
P, P_{eff}, P_f	(Solid rock, effective, pore fluid) Pressure	Pa
q	Heat flux	$W\ m^{-2}$
R	Gas constant	$J\ mol^{-1}\ K^{-1}$
S	S parameter	-
t	Time	s
T	Temperature	K
\mathbf{v}	Velocity	$m\ s^{-1}$
v_p, v_s	P-, S-wave velocity	$m\ s^{-1}$
V	Slip rate	$m\ s^{-1}$
V_a	Activation volume	$J\ Pa^{-1}\ mol^{-1}$
V_c	Characteristic velocity	$m\ s^{-1}$
Z	Seismic impedance	$kg\ s^{-1}\ m^{-2}$

211 $\rho C_p \left(\frac{DT}{Dt} \right)$), and the internal heat generation due to adiabatic (de)compression H_a ,
 212 shear heating during anelastic deformation H_s , and radioactive heat production H_r .

213 We use an implicit finite difference scheme on a fully staggered Eulerian grid
 214 to solve for the velocity \mathbf{v} , the solid rock pressure P , and the temperature T (Gerya
 215 & Yuen, 2007). We use second order spatial discretisation and first order temporal
 216 discretisation. Large deformation is numerically modelled by Lagrangian markers that
 217 are advected according to their velocity, while keeping track of the rock composition,
 218 associated material properties, and stress history (see Gerya & Yuen, 2003, and refer-
 219 ences therein). For a complete description of all the components of the heat equation
 220 used in this model, we refer to van Dinther, Gerya, Dalguer, Mai, et al. (2013).

2.2 Rheology

222 To solve the governing equations, we need constitutive equations that relate the
 223 stress and strain rate. We use a visco-elastic Maxwell rheology in combination with a
 224 frictional plastic slider (Gerya, 2010). The total strain rate is the sum of its elastic,
 225 viscous and plastic components:

$$\dot{\boldsymbol{\epsilon}} = \frac{1}{2} (\nabla \mathbf{v} + \nabla \mathbf{v}^T) = \dot{\boldsymbol{\epsilon}}_v + \dot{\boldsymbol{\epsilon}}_e + \dot{\boldsymbol{\epsilon}}_p. \quad (4)$$

226 The viscous strain rate component is

$$\dot{\boldsymbol{\epsilon}}'_v = \frac{1}{2\eta} \boldsymbol{\sigma}', \quad (5)$$

227 where η is the effective viscosity and $\boldsymbol{\sigma}'$ is the deviatoric stress tensor.

228 The elastic strain rate component is described as

$$\dot{\boldsymbol{\epsilon}}'_e = \frac{1}{2G} \frac{D\boldsymbol{\sigma}'}{Dt}. \quad (6)$$

229 It depends on the shear modulus G and the co-rotational stress rate $\frac{D\boldsymbol{\sigma}'}{Dt} = \frac{\boldsymbol{\sigma}'_{t+1} - \boldsymbol{\sigma}'_t}{\Delta t} +$
 230 $\dot{\boldsymbol{\omega}}\boldsymbol{\sigma} - \boldsymbol{\sigma}\dot{\boldsymbol{\omega}}$, where $\boldsymbol{\omega} = \frac{1}{2} (\nabla \mathbf{v} - \nabla \mathbf{v}^T)$ is the rotation tensor. The SC approach uses
 231 an explicit first-order finite difference scheme to solve for the elastic history. We also
 232 rotate the elastic stresses to account for local stress orientation changes due to the
 233 rotation of material points. More details on the treatment and implementation of
 234 elasticity can be found in Moresi et al. (2003); Gerya (2010); van Dinther, Gerya,
 235 Dalguer, Corbi, et al. (2013); Herrendörfer et al. (2018). The SC numerical method
 236 thus treats elasticity differently from the elastodynamic framework of the DR approach
 237 (Sec. 3). Additionally, the elastic strain rate in the incompressible SC model (Eq. 6)
 238 differs from the compressible formulation in the DR model (Eq. 14).

239 The plastic strain rate component is described as

$$\dot{\boldsymbol{\epsilon}}'_p = \begin{cases} 0 & \text{if } \sigma'_{II} < \sigma_{\text{yield}}^{\text{sc}} \\ \chi \frac{\partial G_{\text{plastic}}}{\partial \sigma'_{II}} & \text{if } \sigma'_{II} = \sigma_{\text{yield}}^{\text{sc}}. \end{cases} \quad (7)$$

240 In this plastic flow rule, G_{plastic} is the plastic potential of yielding material and χ is
 241 the plastic multiplier, which connects the components of the plastic strain rate with
 242 the local stress distribution σ'_{II} .

Table 2. Material parameters seismic cycle model

Material	Rock	Flow law ^a	η_0 [Pa ⁿ s]	n [-]	E_a [J mol ⁻¹]	V_a [J Pa ⁻¹]	ρ_0^b [kg m ⁻³]	G^c [GPa]	μ_s [-]	μ_d^i [-]	C [MPa]
Sticky air	-	-	$1.0 \cdot 10^{17}$	1	0	0	1	700	0	0	0
Incoming sediments	Sediments	Wet quartzite	$1.97 \cdot 10^{17}$	2.3	$1.54 \cdot 10^5$	$0.8 \cdot 10^{-5}$	2600	9.7262	0.35 ^d	0.105	2.5
Sediments	Sediments	Wet quartzite	$1.97 \cdot 10^{17}$	2.3	$1.54 \cdot 10^5$	$0.8 \cdot 10^{-5}$	2600	17	0.35 ^d	0.105	2.5
Upper oceanic crust	Basalt	Wet quartzite	$1.97 \cdot 10^{17}$	2.3	$1.54 \cdot 10^5$	$0.8 \cdot 10^{-5}$	3000	38	0.50 ^e	0.150	5 ^j
Lower oceanic crust	Gabbro	Plagioclase	$4.80 \cdot 10^{22}$	3.2	$2.38 \cdot 10^5$	$0.8 \cdot 10^{-5}$	3000	38	0.85 ^f	0.255	15
Upper continental crust	Sandstone	Wet quartzite	$1.97 \cdot 10^{17}$	2.3	$1.54 \cdot 10^5$	$1.2 \cdot 10^{-5}$	2700	34	0.72 ^g	0.216	10
Lower continental crust	Sandstone	Wet quartzite	$1.97 \cdot 10^{17}$	2.3	$1.54 \cdot 10^5$	$1.2 \cdot 10^{-5}$	2700	34	0.72 ^g	0.216	10
Lithospheric mantle	Peridotite	Dry olivine	$3.98 \cdot 10^{16}$	3.5	$5.32 \cdot 10^5$	$0.8 \cdot 10^{-5}$	3300	63	0.60 ^h	0.180	20
Asthenospheric mantle	Peridotite	Dry olivine	$3.98 \cdot 10^{16}$	3.5	$5.32 \cdot 10^5$	$0.8 \cdot 10^{-5}$	3300	72	0.60 ^h	0.180	20
Mantle weak zone	Peridotite	Wet olivine	$5.01 \cdot 10^{20}$	4.0	$4.70 \cdot 10^5$	$0.8 \cdot 10^{-5}$	3300	63	0.10	0.03	20

See van Dinther, Gerya, Dalguer, Mai, et al. (2013) for parameters related to the energy equation (3). Values obtained from: ^aRanalli (1995) unless otherwise stated; ^bTurcotte and Schubert (2002); ^cBormann et al. (2012); ^dDen Hartog et al. (2012); ^eDi Toro et al. (2011); ^fTsutsumi and Shimamoto (1997); ^ge.g., Dieterich (1978); Chester and Higgs (1992); Di Toro et al. (2011); ^hDel Gaudio et al. (2009); ⁱfriction coefficient decreases to 30% of its initial value μ_s according to Di Toro et al. (2011); ^jSchultz (1995).

243 We consider dislocation creep with a non-linear viscosity η that depends on the
 244 second invariant of the stress tensor σ'_{II} (e.g., Ranalli, 1995):

$$\eta = \left(\frac{1}{\sigma'_{II}}\right)^{n-1} \cdot \frac{1}{2A_D} \cdot \exp\left(\frac{E_a + PV_a}{RT}\right), \quad (8)$$

245 where R is the gas constant and n , A_d , E_a , and V_a are material dependent viscous
 246 parameters (Table 1). Values for the material parameters for each rock type are
 247 constrained by experimental studies and can be found in Table 2.

248 **2.3 Failure criterion and friction formulation**

249 Brittle behaviour is characterised by Drucker-Prager plasticity (Drucker & Prager,
 250 1952), which is commonly used in geodynamics (e.g., Kaus, 2010; Buiter et al.,
 251 2016). In this yield criterion, the second invariant of the deviatoric stress tensor
 252 $\sigma'_{II} = \sqrt{\sigma'^2_{xx} + \sigma'^2_{zz}}$ at a point in the rock is compared to the yield stress (or strength)
 253 $\sigma^{\text{sc}}_{\text{yield}}$ of the rock. Plastic failure in the form of spontaneous brittle instabilities occurs
 254 when the stress reaches the rock's yield stress. The yield stress of a rock depends on
 255 its cohesion C , its friction coefficient μ^{sc} , and the effective pressure P_{eff} , according to

$$\sigma^{\text{sc}}_{\text{yield}} = C + \mu^{\text{sc}} P_{\text{eff}}, \quad (9)$$

256 with P_{eff} defined as

$$P_{\text{eff}} = P - P_f = (1 - \lambda)P, \quad (10)$$

257 where P_f is the pore fluid pressure, such that λ is the pore fluid pressure ratio P_f/P .
 258 The solid rock pressure P is defined as the negative mean stress $-\frac{\sigma_{xx} + \sigma_{zz}}{2}$. We solve
 259 a simplified formulation of fluid flow processes including metamorphic (de)hydration
 260 reactions and compaction (e.g., Gerya & Meilick, 2011). These processes are driven
 261 by pressure, depth, and temperature.

262 We use a strongly slip rate-dependent friction formulation (van Dinther, Gerya,
 263 Dalguer, Corbi, et al., 2013) in which the friction coefficient μ^{sc} drops non-linearly from
 264 the static friction coefficient μ^{sc}_s to the dynamic friction coefficient μ^{sc}_d with increasing
 265 slip rate V , according to

$$\mu^{\text{sc}} = \frac{V_c \mu^{\text{sc}}_s + V \mu^{\text{sc}}_d}{V_c + V}, \quad (11)$$

266 where V_c is the characteristic velocity at which half of the friction drop occurs. The
 267 visco-plastic slip rate V is derived from the visco-plastic strain rate according to

$$V = 2\dot{\epsilon}'_{vp,II} \Delta x, \quad (12)$$

268 where Δx is the minimum grid size.

269 **2.4 Geodynamic seismic cycle model setup**

270 We use a two-dimensional setup of a trench-normal section of the Southern
 271 Chilean subduction zone where the oceanic Nazca plate subducts beneath the con-
 272 tinental South American plate. This setup is based on van Dinther, Gerya, Dalguer,
 273 Mai, et al. (2013) who validated this setup against GPS data before and during the

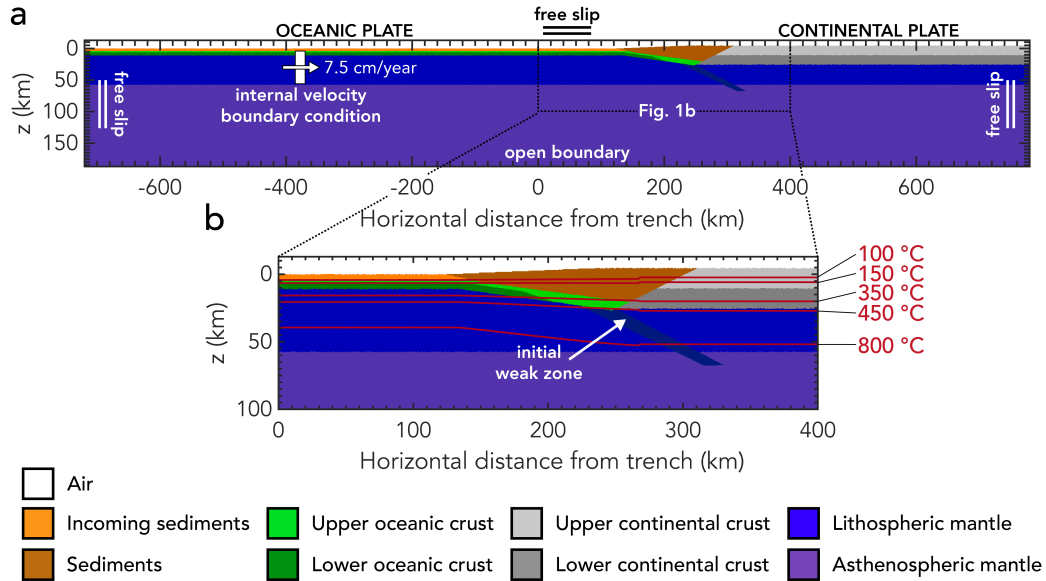


Figure 1. Complete (a) and zoomed (b) model setup of the geodynamic seismic cycle model with lithology (in colour, see key), isotherms (red), and boundary conditions (white). Note that the future trench is located at (0,0) instead of (720, 13) for easy comparison with the other figures in this work.

274 2010 M8.8 Maule earthquake. We consider a $1500 \times 200 \text{ km}^2$ box (Fig. 1) with a
 275 minimum grid size of 500 m in a high resolution area around the megathrust interface.
 276 The high resolution area extends from 0–100 km in the vertical direction and from
 277 650–1225 km in the horizontal direction. In a 50 km region around the high resolution
 278 area, we gradually increase the grid size to 2000 m, which is the maximum grid size
 279 employed in the rest of the model. This results in a grid of 1654×270 nodes. A total
 280 of ~ 54.3 million markers with 20 initial, randomly distributed markers per cell is used
 281 to advect the different materials and their physical properties.

282 The top of the Nazca plate includes a 4 km incoming sediment layer to create
 283 a large accretionary prism in which splay geometries develop. In addition to the
 284 sediment layer, the oceanic Nazca plate consists of a 2 km thick basaltic upper ocean
 285 crust and a 5 km thick gabbroic lower oceanic crust. The initial accretionary wedge
 286 consists of sediments and the continental South American plate consists of a 15 km
 287 thick sandstone upper continental crust and a 15 km thick sandstone lower continental
 288 crust. We use a wet quartzite flow law (Ranalli, 1995) for the continental crust, the
 289 sediments, and the upper oceanic crust; and we use a plagioclase flow law (Ranalli,
 290 1995) for the lower oceanic crust. The two plates overlie an anhydrous, peridotitic
 291 mantle that is approximated with a dry olivine flow law. We use laboratory-derived
 292 material parameters for the different lithologies as described in van Dinther, Gerya,
 293 Dalguer, Mai, et al. (2013), but update cohesion values constrained by e.g., Ranalli
 294 (1995); Schultz (1995), and shear modulus values following Bormann et al. (2012)
 295 (Table 2). While these experimental studies typically report a range of plausible
 296 values, here we choose either a listed reference value or the value typically used in
 297 previous geodynamic modelling studies.

298 We consider long-term fluid flow with a constant pore fluid pressure ratio. At
 299 the start of the model, the ocean floor sediments and oceanic crust contain water.

Regions within 2 km of fluids have an increased pore fluid pressure ratio $\lambda = 0.95$, whereas for dry rocks, the pore fluid pressure ratio $\lambda = 0$. This value of the increased pore fluid pressure ratio is based on observations for Southern Chile (Seno, 2009). The highly over-pressurised pore fluids are primarily required to sustain subduction along a shallow megathrust and obtain reasonable seismic cycle characteristics (van Dinther, Gerya, Dalguer, Mai, et al., 2013). The increased pore fluid pressure ratio results in decreased rock yield stress (Eq. 9). The model does not account for plate (de)hydration reactions for mantle rocks, erosion processes, and serpentinisation.

The seismogenic zone in the SC model develops with the temperature profile of the slab. We impose a velocity-weakening regime when the temperature is higher than 150°C (see Table 2 for lithology-dependent velocity-weakening friction parameters; Blanpied et al., 1995; van Dinther, Gerya, Dalguer, Mai, et al., 2013). Between 100°C and 150°C , there is a transition from velocity-strengthening to velocity-weakening behaviour. The exact switch from velocity-weakening to velocity-strengthening behaviour occurs between the 104°C and 134°C isotherm, depending on rock type and slip rate. We impose a velocity-strengthening regime in the shallow part of the domain when the temperature of the slab is lower than 100°C with the same friction parameters for all rock types with a static friction coefficient $\mu_s^{\text{sc}} = 0.35$ based on sedimentary rocks, a maximum dynamic friction coefficient $\mu_d^{\text{sc}} = 0.875$, and a characteristic slip velocity $V_c = 2 \cdot 10^{-9}$ m/s (see van Dinther, Gerya, Dalguer, Mai, et al., 2013, and references therein for a full derivation of the friction parameters). The downdip limit of the seismogenic zone forms self-consistently due to a brittle-ductile transition that is governed by a decrease in viscosity caused by an increase in temperature.

During the first stage of the model the time step is 1000 years and a suitable subduction geometry is obtained. After 3.6 million years, the time step is gradually reduced to 5 years, which results in the start of the seismic cycle phase of the model after 4.0 million years. We run the seismic cycle phase of the model for ~ 30 thousand years, during which the stresses are initially adapted to seismic cycles. Then, our long run time ensures that we have a long enough observation time to produce robust seismic cycle statistics (van Dinther, Gerya, Dalguer, Mai, et al., 2013).

We use a sticky air approach to approximate a free surface (Cramer et al., 2012). Free slip boundary conditions are used at the top and sides of the model and we have an open boundary condition at the bottom. An internal velocity boundary condition applied to the subducting slab ensures that subduction is initiated and sustained. The initial and boundary conditions we use are the same as in van Dinther, Gerya, Dalguer, Mai, et al. (2013) and are explained in detail in Appendix A, Appendix B and Fig. 1.

3 Dynamic rupture model

We use the two-dimensional version of the software package SeisSol (<http://www.seissol.org>) to solve for earthquake source dynamics coupled to seismic wave propagation (Dumbser & Käser, 2006; de la Puente et al., 2009; Pelties et al., 2014). SeisSol is specifically suited for handling complex geometries due to the use of unstructured triangular computational meshes.

In the following, we shortly summarise the governing equations and frictional failure criterion. The reader is referred to Dumbser and Käser (2006) for a full description of the numerical method and to de la Puente et al. (2009) for details on the implementation of rupture dynamics as an internal boundary condition.

346

3.1 Governing equations

347

348

SeisSol solves the elastic wave equation in a two-dimensional Cartesian coordinate system without external body forces in an isotropic, compressible medium:

$$\rho \frac{\partial \mathbf{v}}{\partial t} = \nabla \cdot \boldsymbol{\sigma} \quad (13)$$

$$\dot{\boldsymbol{\epsilon}}_e = \frac{1}{2G} \frac{\partial \boldsymbol{\sigma}}{\partial t} - \frac{\lambda_1}{2G} \nabla \cdot \mathbf{v}. \quad (14)$$

349

350

351

352

353

354

355

356

357

358

Eq. 13 is the equation of motion. The main difference in the conservation of momentum between the SC and DR model (Eqs. 2 and 13) is that the DR model neglects gravity. While gravity is negligible on the short time scales of elastodynamics, gravity may play a role in the SC model by potentially favouring continued slab subduction. Eq. 14 is the constitutive relation derived from Hooke's law that relates the strain rate to stresses for an elastic, isotropic material (compare Eq. 14 to Eq. 6; look at Eq. 1). Since we only consider an elastic medium in the DR model, the elastic strain rate $\dot{\boldsymbol{\epsilon}}_e$ equals the total strain rate $\dot{\boldsymbol{\epsilon}} = \frac{1}{2}(\nabla \mathbf{v} + \nabla \mathbf{v}^T)$ (compare to Eq. 4). λ_1 and G are the Lamé constants, which determine the Poisson's ratio of the model (Secs. 4.2 and 6.1.1).

359

360

361

362

363

364

365

366

To discretise this set of equations in space, SeisSol uses a Discontinuous Galerkin (DG) method with a Godunov upwind flux, which represents the solution as an exact Riemann problem at the discontinuity between element interfaces (Dumbser & Käser, 2006; de la Puente et al., 2009). Due to the use of triangular mesh elements, this approach is particularly suited for the discretisation of complex geometries like shallow dipping subduction zones, topography or bathymetry. For the discretisation in time, SeisSol uses an Arbitrary high-order DERivative (ADER) method (Dumbser & Käser, 2006).

367

368

369

370

371

372

373

374

Due to the dissipative behaviour of the numerical upwind flux used by SeisSol, spurious high frequency oscillations are subdued in the vicinity of the fault (de la Puente et al., 2009; Pelties et al., 2014; Wollherr et al., 2018). SeisSol is verified with a wide range of two-dimensional and three-dimensional community benchmarks, including strike-slip, dipping and branching fault geometries, laboratory derived friction laws, as well as heterogeneous on-fault initial stresses and material properties (de la Puente et al., 2009; Pelties et al., 2012, 2014; Wollherr et al., 2018) in line with the SCEC/USGS Dynamic Rupture Code Verification exercises (Harris et al., 2011, 2018).

375

3.2 Failure criterion and friction formulation

376

377

378

379

We incorporate frictional failure as an internal boundary condition of the element edges associated with the fault, which is meshed explicitly. Fault slip in the DR model is therefore restricted to this fault line in contrast to the SC model where the entire domain is theoretically allowed to slip.

380

381

382

383

384

To check the Coulomb failure criterion, the stress tensor, which consists of the initial stress and any subsequent stress change, is rotated into the fault coordinate system defined by the normal and tangential vectors of each fault point. The DR model compares the absolute shear stress $|\tau|$ on the fault to the fault yield stress $\sigma_{\text{yield}}^{\text{dr}}$:

$$\sigma_{\text{yield}}^{\text{dr}} = C + \mu_s^{\text{dr}} \sigma_n. \quad (15)$$

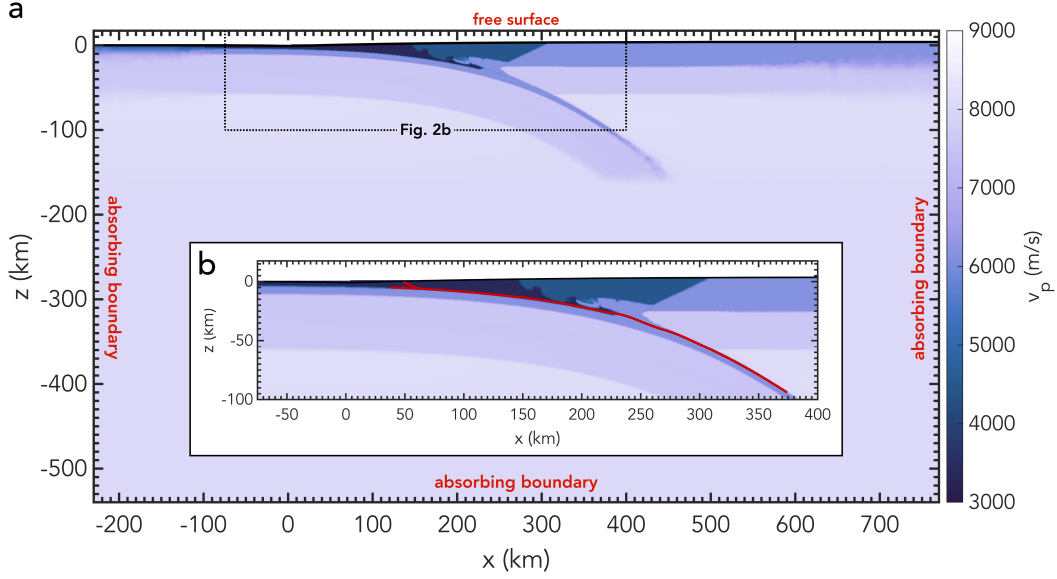


Figure 2. Complete (a) and zoomed (b) model setup of the dynamic rupture model with P-wave velocity v_p (in colour; Table 3), boundary conditions (red) and megathrust and splay fault geometry (red lines). The splay fault is always explicitly meshed in the DR model, but the frictional boundary condition on the splay fault is only activated for the model in Sec. 5.6.

385 It consists of the fault cohesion C , the static friction coefficient μ_s^{dr} , and the normal
 386 stress σ_n (compare to Eq. 9). If the shear stress overcomes the fault's yield stress, the
 387 fault fails and its strength becomes $\sigma_{\text{sliding}}^{\text{dr}}$:

$$\sigma_{\text{sliding}}^{\text{dr}} = \mu^{\text{dr}} \sigma_n. \quad (16)$$

388 During sliding, the friction coefficient μ^{dr} is governed by a linear slip weakening friction
 389 law (Ida, 1973). For this constitutive law, μ^{dr} decreases linearly from its static value
 390 μ_s^{dr} to its dynamic value μ_d^{dr} with slip distance Δd over a specified critical slip distance
 391 D_c , i.e.

$$\mu^{\text{dr}} = \begin{cases} \mu_s^{\text{dr}} - \frac{\mu_s^{\text{dr}} - \mu_d^{\text{dr}}}{D_c} \Delta d & \text{if } \Delta d < D_c \\ \mu_d^{\text{dr}} & \text{if } \Delta d \geq D_c. \end{cases} \quad (17)$$

392 Slip produces seismic waves. When failure occurs on the fault, the rupture front
 393 and the emitted seismic waves can influence the tractions on the fault. These can
 394 bring the fault closer to failure when the normal traction decreases and/or the shear
 395 traction increases. It can move the fault further away from failure if the normal traction
 396 increases and/or the shear traction decreases.

397 3.3 Dynamic rupture model setup

398 The DR modelling domain is a 575 km wide and 169 km deep subsection of
 399 the SC domain (Fig. 2). We copy the SC material properties at the boundaries of
 400 this domain to extend the DR simulation domain to 1000 km width and 544 km
 401 depth to avoid artificial wave reflections from the boundaries. Copying the values
 402 is necessary, because of the limited depth of the SC model and the interference of

Table 3. Seismic velocities dynamic rupture model

Material	v_p [m s ⁻¹]	v_s [m s ⁻¹]
Incoming sediments	3350	1934
Sediments	4429	2557
Upper oceanic crust	6164	3559
Lower oceanic crust	6164	3559
Upper continental crust	6146	3549
Lower continental crust	6146	3549
Lithospheric mantle	7568	4369
Asthenospheric mantle	8090	4671

403 boundary conditions with the material parameters and physical variables close to the
 404 domain edges. The fault geometry is extracted from the SC model according to the
 405 region of highest visco-plastic strain rate during the SC coupling event (see Sec. 4.4).

406 For the dynamic rupture simulations we use a 6th order spatial and temporal
 407 discretisation. We use the open source software Gmsh (Geuzaine & Remacle, 2009) to
 408 generate the mesh. The nodal grid size at the fault is 200 m and is gradually coarsened
 409 to 2.5 km at the edges of a high resolution domain with the same dimensions as the SC
 410 subsection domain. Outside this area, we apply rapid coarsening to 50 km at the edges
 411 of the larger domain to disseminate the non-perfect absorbing boundary conditions.
 412 Note that the fault is additionally subsampled by six Gaussian integration points which
 413 increases the resolution on the fault to 33.3 m. The corresponding mesh consists of
 414 543'048 elements.

415 To ensure stability of the numerical scheme, the time step is calculated in de-
 416 pendence of the Courant-Friedrichs-Lewy criterion using $C_{CFL} = 0.5$ (de la Puente et
 417 al., 2009), the minimum insphere over all mesh elements, and the fastest wave speed
 418 v_p . This leads to a time step of $7.5 \cdot 10^{-5}$ s.

419 Element-wise values for friction parameters, initial stress and yield stress, and
 420 rock properties with seismic velocities listed in Table 3, are obtained from the SC
 421 model as described in Sec. 4.

422 We approximate the maximum resolved frequency in our model f_{\max} according
 423 to de la Puente et al. (2009):

$$f_{\max} = \frac{v_{\min}}{1.45\Delta x} \quad (18)$$

424 which is valid for a 4th order discretisation scheme. Here, v_{\min} is the minimum velocity
 425 in the model (i.e., the shear velocity of the incoming sediments) and Δx is the grid
 426 size. The maximum resolved frequency varies from 6.67 Hz on the fault to 0.53 Hz at
 427 the edges of the high resolution domain. As we use a 6th order discretisation, we are
 428 able to resolve even higher frequencies. These frequencies are well within the range of
 429 typical dynamic rupture models (e.g., Wollherr, Gabriel, & Mai, 2019), so our analysis
 430 is well resolved.

431 We use a free surface boundary condition, which sets shear and normal stresses to
 432 zero in the absence of external forces. Additionally, the model uses absorbing boundary

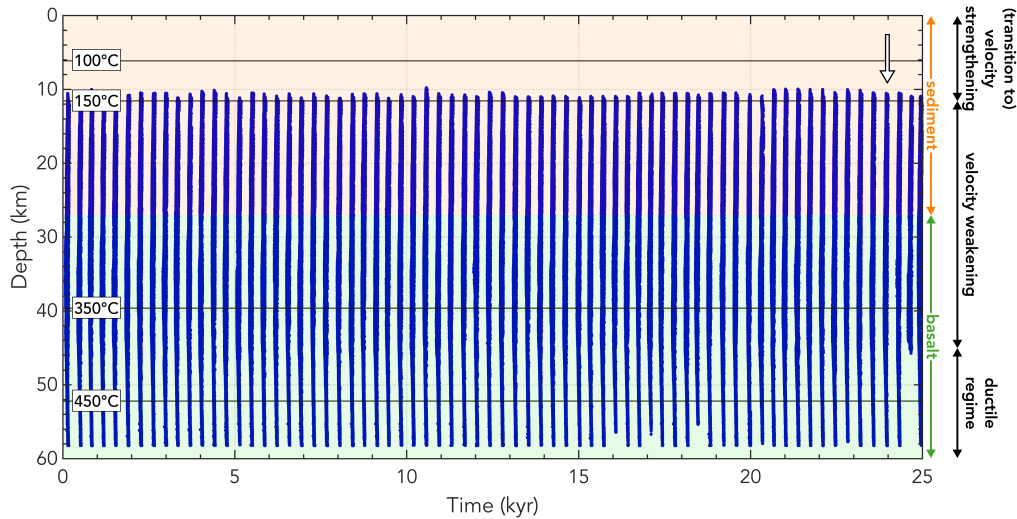


Figure 3. Space-time evolution of the SC model of subduction zone seismicity. Each dot (closely clustered together to form lines) represents a marker that satisfies our Rupture Detector Algorithm thresholds (see text; Dal Zilio et al., 2018). The event that we use as the SC coupling event for our SC to DR coupling is indicated by the arrow. Frictional regimes dependent on temperature are indicated with corresponding isotherms (solid black lines). Background colours represent the rock type through which the fault is going.

433 conditions which reduce the reflections of outgoing waves at the domain boundaries
 434 (Dumbser & Käser, 2006).

435 **4 Coupling method**

436 In this section, we discuss the resulting long-term seismicity characteristics of the
 437 SC model and how we choose an event from the SC model to couple to the DR model.
 438 We then show how we couple the material properties of the domain, the stresses,
 439 the fault geometry, and yield criteria in the two modelling approaches. The full SC
 440 results used for coupling to the dynamic rupture model are included in the Supporting
 441 Information and can be used as input for other dynamic rupture models.

442 **4.1 Long-term seismic cycle characteristics and selection of coupling time** 443 **step**

444 In the seismic cycle phase, we observe 70 spontaneous quasi-periodic megathrust
 445 events (Fig. 3). To quantify their characteristics we apply a minimum slip rate thresh-
 446 old of $2.5 \cdot 10^{-9}$ m/s and a minimum stress drop threshold of 0.4 MPa on all markers
 447 (Dal Zilio et al., 2018). Most events rupture almost the entire megathrust apart from
 448 the shallow, velocity-strengthening part. The exact rupture path is different for each
 449 event, because of the different stress and strain distributions for each event in the
 450 broad subduction channel and accretionary wedge. This is particularly true in the
 451 downdip region of the seismogenic zone where the rupture paths sometimes deviate
 452 from the rock interfaces. In the shallow part of the subduction zone, the sediments
 453 are favoured over the basalt for rupture propagation, due to their lower yield stress
 454 (Table 2). The average recurrence interval of the megathrust events is approximately
 455 270 years, which is in line with estimates of the recurrence interval in Southern Chile
 456 (e.g., Cisternas et al., 2005).

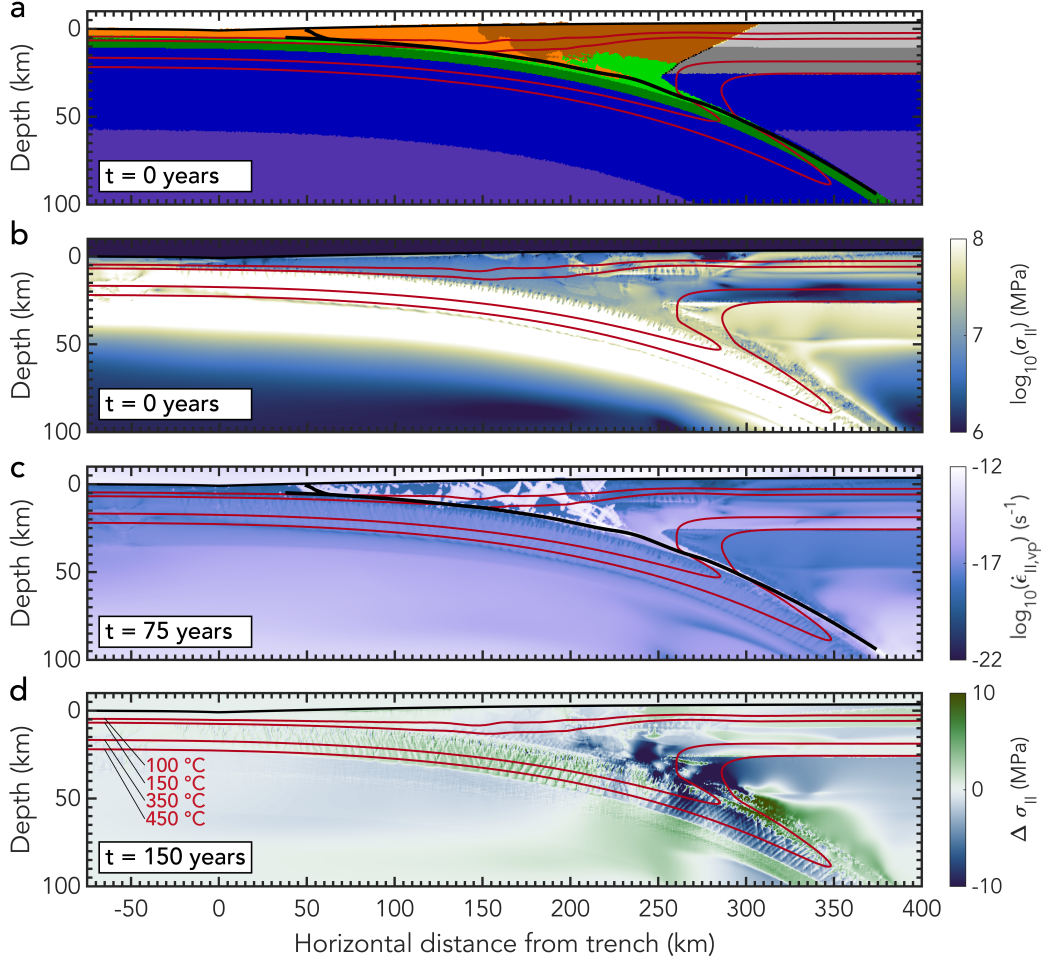


Figure 4. Representative coupling event of the geodynamic seismic cycle model. (a) Lithological structure after 4 Myr (compare to Fig. 1) at the start of the event ($t = 0$ years) with the fault indicated in black. (b) Initial stress used as input for the DR model. (c) Strain rate during the event at 75 years from the start of the event with the fault indicated in black. (d) Stress change with respect to the initial stress in (b) towards the end of the event 150 years from the start. Isotherms that define the frictional regimes and hence seismogenic zone are indicated in red. The boundary between rocks and sticky air is highlighted with a thick solid black line.

457 We choose the rupture indicated by the arrow in Fig. 3 as the SC coupling event
 458 that we import to the dynamic rupture model. The chosen event is representative for
 459 other events in terms of its duration and stress drop and it has a smooth rupture path.
 460 The geometry resulting from ~ 4 Myr subduction consists of a large accretionary wedge
 461 created by the incoming sediments and a slab with an average dip of 14° (Fig. 4a). At
 462 the initiation of the rupture, stress has built up during the interseismic stage in the
 463 lower part of the seismogenic zone (Fig. 4b). Like all other events in the SC model, this
 464 event also results in a lot of yielding in the shallow part of the accretionary wedge as
 465 shown by the strain rate localisation in Fig. 4c. This large yielding region represents the
 466 large-scale failure of the unconsolidated accretionary wedge, which contains multiple
 467 possible splay fault geometries. Although the localisation of strain on the splay faults
 468 and the megathrust is simultaneous, the splay faults are not detected as part of an
 469 event, because their lower slip velocity is below the threshold and on the order of
 470 $0.1 \cdot 10^{-9}$ m/s to $1 \cdot 10^{-9}$ m/s. The resulting stress change of the SC event in Fig. 4d
 471 shows a stress drop in the subduction channel, particularly near the downdip limit of
 472 the seismogenic zone.

473 We need to choose the coupling time step of the SC coupling event for which we
 474 import the conditions from the SC model to the DR model as initial conditions. For
 475 this coupling time step we export the rock properties, friction coefficient and stresses
 476 to the DR model, as discussed in the following sections. We also use this time step as
 477 the start of the SC event, so that we can use it and the subsequent time steps that
 478 comprise the entire SC event to determine the fault geometry and dynamic friction
 479 coefficient.

480 We select the first time step of the coupling event in the SC model for which
 481 nucleation and subsequent propagation of the rupture occurs spontaneously in the DR
 482 model in order to stay as close to the SC model as possible. This time step corresponds
 483 to the time step at which failure occurs in the SC model on two adjacent fault points.

484 4.2 Lithological structure

485 Density, shear modulus, and cohesion are directly transported into the DR model.
 486 The sticky air material, which is used for the free surface approximation in the SC
 487 model, does not enter the DR model, which has a true free surface boundary condition.
 488 To provide the DR model with a smooth surface and purely rock-related properties
 489 (i.e., no sticky air), we first approximate the air-rock boundary of the SC model with
 490 a 3rd order polynomial that is used as the free surface geometry of the DR model. All
 491 parameters, including material properties, stresses, and friction values associated with
 492 small sticky air patches residual from the free surface interpolation are then replaced
 493 by the corresponding parameters of the underlying rock to prevent any of the sticky
 494 air properties to enter the DR model.

495 The SC model assumes incompressible materials, i.e., Poisson's ratio $\nu = 0.5$.
 496 In the DR model, the material is compressible, so $\nu \neq 0.5$. We choose $\nu = 0.25$ to
 497 calculate the first Lamé parameter λ_1 from the shear modulus G in the SC model.
 498 This value of Poisson's ratio is based on the simplifying assumption that rocks can be
 499 treated as Poisson solids with $\lambda_1 = G$ (Stein & Wysession, 2009). We discuss possible
 500 variations of Poisson's ratio and its influence on the rupture dynamics in Sec. 6.1.

501 4.3 State of stress

502 As the stress in the SC model consists of elastic, viscous, and plastic components,
 503 it is important to establish the main deformation mechanism at the coupling time step
 504 before transporting the stresses to the fully elastic DR model. We analyse the visco-
 505 elasticity factor F at the coupling time step to determine the dominant deformation

mechanism (Appendix C). We find that the deformation mechanism in the seismogenic zone (i.e., between temperatures of 150°C and 350°C) of the SC model is elastic behaviour, which results in stresses with an almost purely elastic component (i.e., $F < 0.05$; Appendix C; Fig. C1). At temperatures higher than 350°C, the deformation mechanism in the subduction channel slowly starts to include a viscous component as a result of dislocation creep. This change in deformation mechanism effectively defines the downdip limit of the seismogenic zone.

Hence, we mainly transport elastic stresses from the visco-elasto-plastic SC model to the elastic DR model in the seismogenic zone. Exporting the stresses from the SC model to the DR model ensures that the stress history from the SC model is preserved in the DR model on the fault. The stresses then continue to evolve during the dynamic rupture in the DR model.

The SC model uses deviatoric stresses σ' , like many other geodynamic models, whereas the DR model uses non-deviatoric stresses. The two models also use different sign and coordinate conventions (more details in the Supporting Information), so the stresses from the SC model need to be converted to the conventions of the DR model.

First, the deviatoric stresses σ'^{sc} of the SC model are converted to non-deviatoric stresses σ^{sc} according to

$$\sigma^{sc} = \begin{pmatrix} \sigma_{xx}^{sc} & \sigma_{xz}^{sc} \\ \sigma_{xz}^{sc} & \sigma_{zz}^{sc} \end{pmatrix} = \begin{pmatrix} \sigma'^{sc}_{xx} - P & \sigma_{xz}^{sc} \\ \sigma_{xz}^{sc} & -\sigma'^{sc}_{xx} - P \end{pmatrix}, \quad (19)$$

where P is the solid rock pressure.

Besides that, we need to take into account the different coordinate systems with the z -axis pointing downwards for the SC model and upwards for the DR model. The two models also have opposite stress conventions for both the diagonal and shear components of the stress tensor (see the Supporting Information for details). To account for this, we use the following stress tensor as input for the DR model:

$$\sigma^{dr} = \begin{pmatrix} -\sigma_{xx}^{sc} & \sigma_{xz}^{sc} \\ \sigma_{xz}^{sc} & -\sigma_{zz}^{sc} \end{pmatrix}. \quad (20)$$

We use bilinear interpolation to map the SC stress field from the regular SC grid onto the sub-elemental Gaussian integration points along the edges of all triangular elements holding a dynamic rupture boundary condition. Based on the fault orientation, the shear and normal tractions on the fault are then determined to evaluate the yield criterion in the DR model (Eq. 15).

4.4 Fault geometry

In the SC model we use Drucker-Prager plasticity to approximate the brittle failure in a continuous medium (Eq. 9). Plastic yielding of the SC model manifests itself in the localisation of strain rate in shear bands, which we interpret as faults. Therefore, the SC model has no pre-defined, discontinuous fault surfaces to which fault slip is explicitly restricted. Instead, fault orientations are determined by the local stress field (Preuss et al., 2019) and fault slip rate and slip are calculated from local, visco-plastic strain rates assuming one grid cell wide faults (e.g., van Dinther, Gerya, Dalguer, Mai, et al., 2013). In contrast, the DR model uses the elastic Coulomb criterion (Eq. 14) to describe failure on pre-existing, infinitely thin, discontinuous fault interfaces.

As the fault geometry in the DR model needs to be predefined, we have to define a localised, infinitely thin fault line from the SC model. Therefore, we look at the

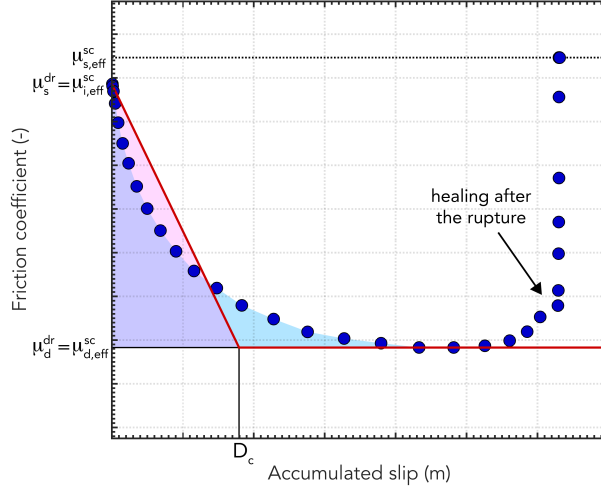


Figure 5. Illustration of the linear slip weakening approximation of rate-dependent friction for one fault point. Each blue dot represents the effective friction coefficient and corresponding accumulated slip for one time step of the SC model during the entire rupture. The final picked μ_s^{dr} , μ_d^{dr} , and D_c are indicated by solid black lines. The final linear slip weakening approximation is indicated in red. D_c is calculated by ensuring that the friction drop during slip of the linear slip weakening law (pink area underneath red line) equals the friction drop during slip of the rate-dependent friction law (blue area underneath blue dots). The area is purple where these two areas overlap. Note that the static friction coefficient of the DR model is not necessarily equal to that of the SC model, but instead equals the SC friction coefficient at the start of the event $\mu_{i,\text{eff}}^{\text{sc}}$.

548 coupling time step of Sec. 4.1 and the 43 subsequent time steps that make up the SC
 549 event. We pick the z -coordinate with the highest visco-plastic strain rate during the
 550 entire SC slip event for each nodal x -coordinate (Fig. 4c). We smooth the fault with
 551 a moving average low-pass filter scheme with a span of 25 points to avoid stair-casing
 552 effects due to the rectangular discretisation and low resolution of the SC model. This
 553 ensures that the nucleation region is correctly represented in the fault geometry.

554 The SC fault geometry reveals that a shallow splay fault is preferred over the
 555 megathrust in the velocity-strengthening region (Figs. 2 and 4). For simplicity, our
 556 models initially only contain the megathrust, which is manually extended by adding
 557 ~ 25 km updip of the fault with the constant dip from the shallowest part of the
 558 megathrust. The total length of the megathrust is then 351.3 km with an average dip
 559 of 14.3° and a minimum and maximum dip of 2.3° and 34.4° , respectively. The splay
 560 fault is connected to the megathrust at $x = 24.5$ km along the megathrust. It has a
 561 length of 14.6 km with an average dip of 21.1° and a minimum and maximum dip of
 562 8.1° and 36.8° , respectively. This splay fault is included in the mesh for all DR models
 563 to ensure that the results of adding a splay fault in Sec. 5.6 are not influenced by any
 564 changes in the mesh. In Sec. 5.6, the frictional boundary condition on the splay fault is
 565 activated, so that slip on the splay fault is theoretically possible. In all other models,
 566 the frictional boundary condition on the splay fault is turned off.

567 4.5 Yield criteria

568 Yielding and slip in the SC and DR models are governed by different physical
 569 mechanisms. The static friction in the SC model is an internal friction coefficient that

570 is a material property inherent to the host rock, whereas the static friction coefficient
 571 in the DR model is a frictional property assigned only to the fault. However, internal
 572 and on-fault friction coefficients have the same range of possible values (e.g., Tables
 573 9.5 and 9.7 in Pollard et al., 2005) and may be assumed to be equal (e.g., Gabriel et
 574 al., 2013).

575 We translate the SC yield criterion to the DR model by equating Eqs. 9 and 15.
 576 We then assume that cohesion can be mapped directly from the SC model to the DR
 577 model. Assuming that the magnitude of the pressure or mean stress P , is equal to the
 578 magnitude of the effective normal traction, σ_n , we can couple the friction coefficients
 579 according to

$$\mu^{\text{dr}} = \mu_{\text{eff}}^{\text{sc}} = (1 - \lambda)\mu^{\text{sc}}. \quad (21)$$

580 Hence, the presence of pore fluids, with a pore fluid pressure ratio $\lambda = 0.95$,
 581 reduces the effective friction coefficient in the SC model (Sec. 2.4). We observe an
 582 average difference of 7 MPa between SC pressure and DR normal tractions, which is
 583 negligible compared to their absolute magnitudes in the range of GPa's. An advantage
 584 of this coupling is that the on-fault friction coefficients vary in dependance of rock type
 585 throughout the DR model. The effective friction coefficients range from 0.028 to 0.005
 586 and are in line with theoretical estimates (e.g., Wang & Hu, 2006) and experiments
 587 (e.g., Kopf & Brown, 2003; Ujiie et al., 2013).

588 We import the current friction coefficient μ_i^{sc} of our coupling time step as the
 589 initial, static friction coefficient for the DR model. We use the minimum friction
 590 coefficient μ_d^{sc} that is reached during the event in the SC model as the DR dynamic
 591 friction coefficient. The corresponding characteristic slip distance D_c is then calculated
 592 such that the area of the strength drop during slip of the linear slip weakening law
 593 equals the area of the strength drop during slip of the rate-dependent friction law:

$$D_c = \frac{2}{\mu_s^{\text{dr}} - \mu_d^{\text{dr}}} \sum_{t=1}^{t_{\text{max}}} (d_t - d_{t-1}) \cdot \left(\mu_{\text{eff},t}^{\text{sc}} + \frac{1}{2} \mu_{\text{eff},t-1}^{\text{sc}} - \mu_d^{\text{dr}} \right). \quad (22)$$

594 Here, $t = 0$ is the coupling time step (Sec. 4.1), t_{max} is the time step in the SC model
 595 at which the lowest friction coefficient is obtained, d is the accumulated slip for a given
 596 point in time and the SC friction coefficients are the effective friction coefficients. Also
 597 note that $\mu_d^{\text{dr}} = \mu_{d,\text{eff}}^{\text{sc}}$. Fig. 5 illustrates this friction law approximation for one fault
 598 point, with the data from the SC model plotted as blue dots and the corresponding
 599 linear slip weakening approximation for the DR model in red.

600 Using this approach, we get a self-consistent approximation in the DR model of
 601 the velocity-strengthening behaviour in the shallow part of the SC model by having
 602 $\mu_d^{\text{dr}} > \mu_s^{\text{dr}}$.

603 We use the same bilinear interpolation scheme used for the SC stress field to map
 604 the friction coefficients and the cohesion onto the DR fault.

605 5 Results and analysis

606 In this section, we first describe the on-fault stress state that results from the
 607 SC model in Sec. 5.1. We then describe the results from the SC event (Sec. 5.2) and
 608 the corresponding DR rupture (Sec. 5.3) in detail and compare them (Sec. 5.4). In
 609 Sec. 5.5, we study the effect of complex lithological structures on the resulting rupture
 610 through a series of increasingly complex models studies. Lastly, we analyse how a
 611 splay fault affects the dynamic rupture in Sec. 5.6.

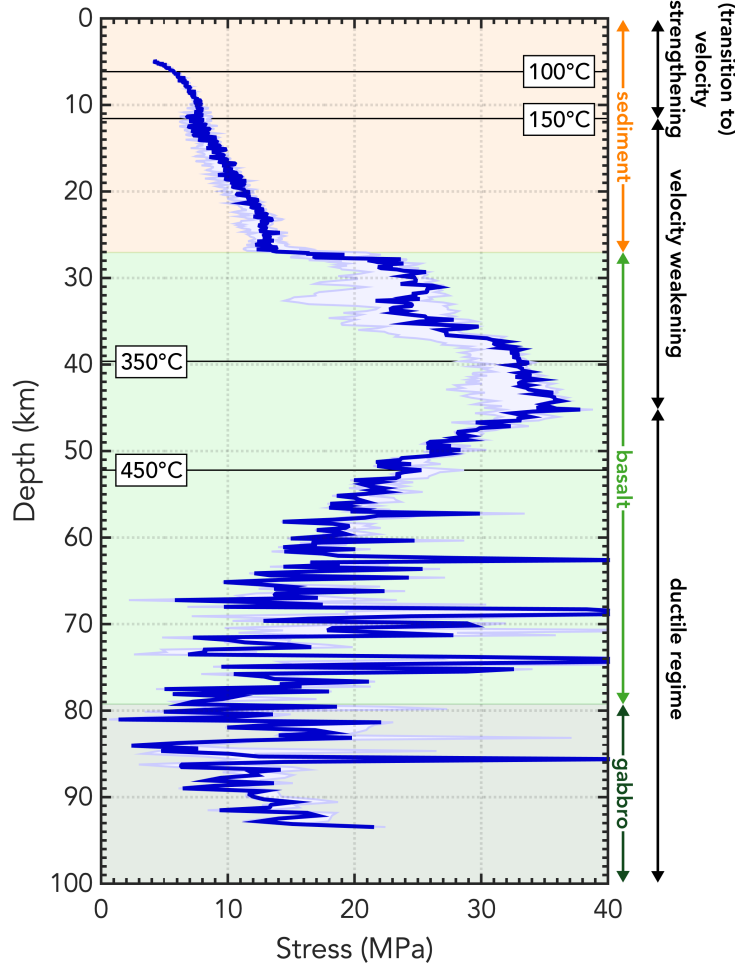


Figure 6. Variability of the stress σ'_{II} at the time of nucleation indicated by the light blue shaded area with the initial stress of the reference model indicated by the blue line. Frictional regimes dependent on temperature are indicated with corresponding isotherms (solid black lines). Background colours represent the rock type through which the fault is going.

612

5.1 Long-term constrained state of stress of the megathrust

613

614

615

616

617

618

619

620

621

622

623

624

Fig. 6 shows the variability of the on-fault stress σ'_{II} which is used in the SC failure criterion (Eqs. 7 and 9) for the 14 events during the last 5000 years of simulation time of the SC model. It is calculated by obtaining the minimum and maximum stress for each fault point from 10 time steps around the nucleation time. For simplicity, we used the fault geometry of the coupled SC event (Sec. 4.4), although the actual fault geometries of other events might deviate from that of the coupled event (van Dinther, Gerya, Dalguer, Mai, et al., 2013). We visualise variables of the SC model on the discrete DR fault (Sec. 4.4) by using the values of the neighbouring grid cell with the highest strain rate for each fault point, which approximates the fault of the SC event optimally. As the rupture path changes for each event, this leads to slight deviations in individual stress profiles, but it does not change the overall stress variability, i.e., the minimum and maximum possible initial stress at a fault point.

625

626

The stress profiles in Fig. 6 all show a similar trend in terms of stress distribution along the fault with depth and the amount of stress heterogeneity. There is no

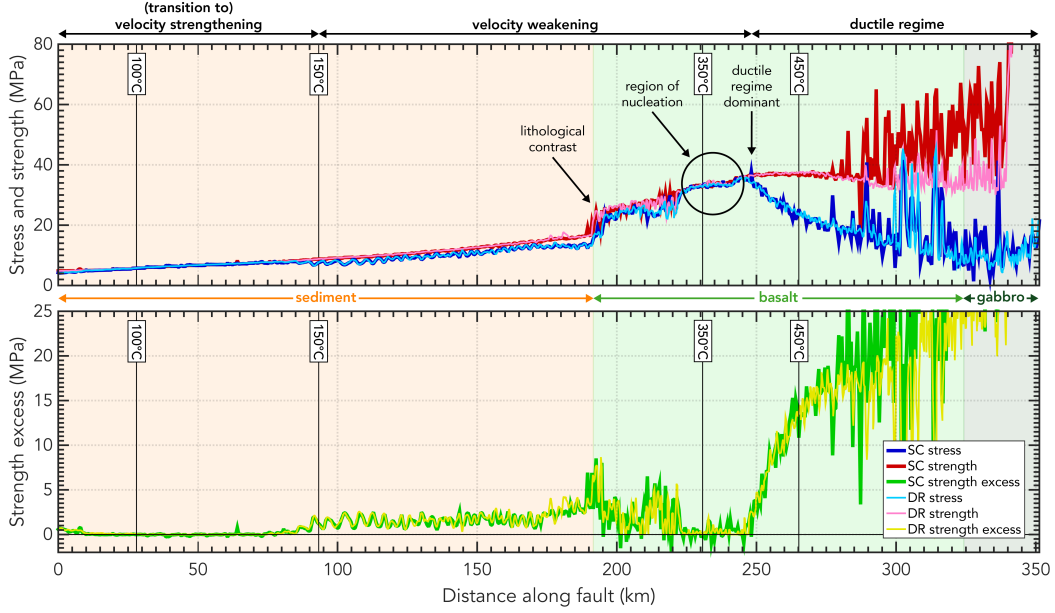


Figure 7. Failure analysis of the SC model at the coupling time step and thus the initial conditions of the DR model along the fault. Second invariant of the deviatoric stress tensor σ'_{II} , yield stress $\sigma_{\text{yield}}^{\text{sc}}$, and strength excess $\sigma_{\text{yield}}^{\text{sc}} - \sigma'_{II}$ for the SC model (bold lines); and initial shear stress τ , fault yield stress $\sigma_{\text{yield}}^{\text{dr}}$, and strength excess $\sigma_{\text{yield}}^{\text{dr}} - \tau$ for the DR model (thin lines) in the fault coordinate system. Frictional regimes dependent on temperature are indicated with corresponding isotherms (solid black lines). Background colours represent the material through which the fault is going.

627 stress variability in the upper part of the sediments where the velocity-strengthening
 628 regime dominates. This is due to the fact that the events do not propagate on this
 629 part of the fault, but instead choose a splay fault over the megathrust in the velocity-
 630 strengthening region (Sec. 4.4). There is little variation in the velocity-weakening
 631 regime of the sediments. There is no sharp transition between sediments and basalt,
 632 but instead the two materials are intermixed. This results in a high stress variability
 633 in the shallow part of the basaltic region indicated in Fig. 6. The stress variability
 634 becomes larger in the basalt with the maximum difference in nucleation stress at a
 635 given fault point being 11.5 MPa. There is a peak in the stresses at the downdip end
 636 of the seismogenic zone below the 350°C isotherm. This is the nucleation region of
 637 most of the SC events. Here, the stress build-up is largest, because the differential
 638 displacement between the locked seismogenic zone and the creeping viscous domain is
 639 largest. In the ductile regime starting at 45 km depth, the stresses decrease by viscous
 640 relaxation related to the dislocation creep (Fig. 6). The spontaneous brittle-ductile
 641 transition occurs, because the viscosity of the materials gradually decreases by several
 642 orders of magnitude due to an increase in temperature with depth (Eq. 8). The exact
 643 location of the transition is governed by the laboratory-derived viscous parameters
 644 in the wet quartzite flow law (Table 2). In the ductile regime, the stress variability
 645 between events is small, but all stress fields show the same highly heterogeneous behav-
 646 iour. These stress heterogeneities are mainly caused by the close proximity and
 647 intermittent presence of mixed pockets of basalt, gabbro and mantle. These lithologies
 648 have different viscous flow law parameters and thus have a different viscosity for the
 649 same temperature and pressure conditions. This leads to distinct differences in stress
 650 build-up and relaxation, which causes a highly heterogeneous stress state.

651 Fig. 7 focuses on the stress and strength conditions for the coupled event to
 652 analyse where failure is occurring in each of the models. According to their failure
 653 criterion, the SC model compares the initial second invariant of the deviatoric stress
 654 tensor σ'_{II} with the yield stress $\sigma'_{\text{yield}}^{\text{sc}}$ of the rock, whereas the DR model compares the
 655 initial shear stress τ to the fault yield stress $\sigma'_{\text{yield}}^{\text{dr}}$. In the following sections, the term
 656 “stress” is generally used to refer to both σ'_{II} and τ , and “yield stress” is used to refer
 657 to $\sigma'_{\text{yield}}^{\text{sc}}$ and $\sigma'_{\text{yield}}^{\text{dr}}$.

658 The values for the second invariant of the deviatoric stress $\sigma'_{II} = \sqrt{\sigma'^2_{xx} + \sigma'^2_{zz}}$
 659 in the SC model range from 1.4 MPa to 37.8 MPa. In the shallow part of the fault,
 660 where the fault is embedded in the sediments of the accretionary wedge, the stress
 661 and yield stress are close, which reflects the constant closeness to failure of creeping
 662 patches during the interseismic period. The proximity of sediments and basalt in the
 663 subduction channel results in a material change on the fault with a corresponding stress
 664 and yield stress change, as these two materials have different elastic moduli, friction
 665 and cohesion values (Fig. 4 and Table 2). The stress and yield stress variability between
 666 192 and 223 km along the fault is large, because there are isolated patches of subducted
 667 sediments in the basalt close to the fault that locally affect the stress and yield stress
 668 on the fault. The nucleation region is located in the basaltic region near the down-dip
 669 limit of the seismogenic zone. For the chosen coupling time step from the SC model,
 670 stress reaches the yield stress of the basalt at the nucleation region ~ 225 – 245 km along
 671 the fault. The peak stress in the basalt reaches 37.8 MPa. The stresses drop when the
 672 viscous behaviour becomes dominant at 248 km along the fault. The material change
 673 from basalt to gabbro is not accompanied by a distinct change in stress or yield stress.
 674 This is because the frictional properties no longer dictate the stress and yield stress
 675 of the rock in the ductile regime. The oscillations of the stress and yield stress in the
 676 ductile regime are caused by material heterogeneity. Smaller oscillations, as observed
 677 in the sediment and basalt are due to mapping the SC properties on the discrete DR
 678 fault with the nearest neighbour interpolation.

679 5.2 Geodynamic seismic cycle slip event

680 Fig. 8 shows the on-fault evolution of slip rate during both the SC and DR
 681 events through space and time. Important features are indicated by numbers, which
 682 are discussed in this and the following section.

683 The slip rate of the SC model in Fig. 8a shows the initial nucleation phase
 684 indicated by (1) during which slip rates are still low $V < 1.0 \cdot 10^{-9}$ m/s. After
 685 ~ 50 years, the rupture starts propagating mainly updip until it is stalled when entering
 686 the velocity-strengthening region (2) and the ductile regime (3), respectively. The
 687 highest slip rates of $5.7 \cdot 10^{-9}$ m/s are reached in the sediments. There is continuous
 688 creeping on the fault in the ductile regime with slip rates of $\sim 3 \cdot 10^{-10}$ m/s. The SC
 689 event lasts for 180 years due to the 5 year time step and the low characteristic velocity
 690 in the slip rate-dependent friction formulation. The low slip rate during the rupture on
 691 the order of 10^{-9} m/s is a direct result of this. Note that due to the evaluation of this
 692 event with the nearest neighbour interpolation at the fault geometry approximation
 693 adopted for the DR model, we see visual artefacts in the form of stripes (4) in Figs. 8a,b.
 694 Similar artefacts are introduced in the DR coupling by the interpolation of the coarse
 695 SC model resolution variables onto the high resolution DR fault.

696 The corresponding stress change along the fault with respect to the initial stress
 697 of the event over time always shows a stress increase (1) ahead of the rupture front due
 698 to the conservation of momentum (Fig. 8b). We observe a maximum stress drop over
 699 time of 15 MPa in the nucleation region. The stress drop is material dependent, as the
 700 stress drop in the basalt is 9.4 MPa on average, whereas the average stress drop of the
 701 sediments is 2.8 MPa. We find an average stress drop of 5.6 MPa between the 150°C

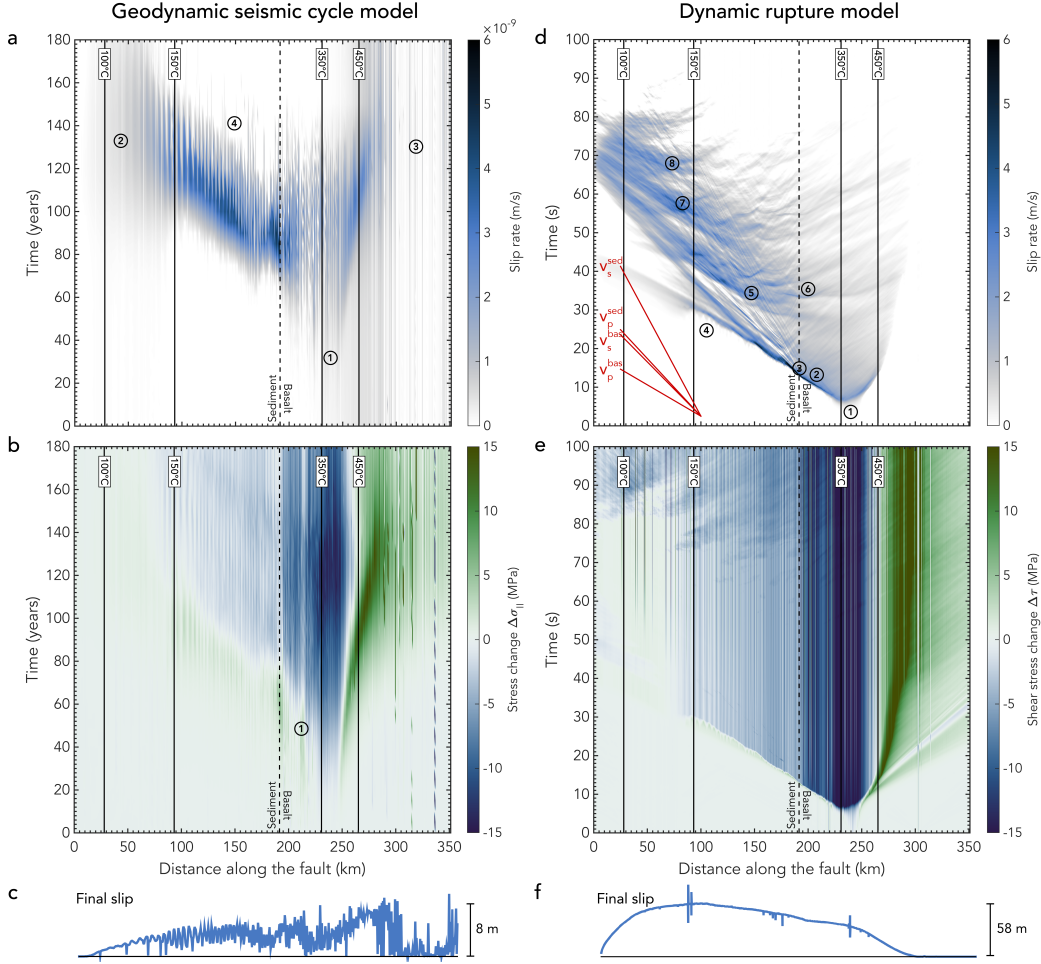


Figure 8. Slip rate evolution with time (a,d), temporal stress change evolution (b,e), and final accumulated slip (c,f) along the fault for the same rupture in the SC model (left column) and the DR model (right column). Solid lines indicate the isotherms that define the frictional regimes; dotted line indicates material change. The P- and S-wave velocities v_p and v_s for both the basalt (_{bas}) and sediment (_{sed}) are indicated in red. Numbers are discussed in the text. We take $t = 0$ years in the SC model for the time step at which we transfer the stresses. The oscillating behaviour visible in the SC final slip distribution stems from the visualisation of the interpolation of the continuous SC model on the discrete DR fault. Low slip rates and high stress drop near the nucleation region likely show the approximated fault does not capture the main slip patch there. Peak slip is indicated.

and 450° isotherms. When the frictional regime transitions from velocity-weakening to velocity-strengthening at the updip limit of the seismogenic zone, the stress drop becomes very small.

The final slip distribution in Fig. 8c shows high slip with a maximum of 8.3 m in the deeper part of the seismogenic zone, which decreases towards the trench and the ductile regime. Note that slip below the 450° isotherm is largely the result of continuous, ductile creep.

5.3 Coupled dynamic rupture event

The initial conditions imported from the SC model result in the spontaneous nucleation of an earthquake within the DR model (Fig. 8d, (1)) without using any artificial nucleation procedures. The nucleation phase before the spontaneous rupture propagation lasts for ~ 6.5 s and results in a large nucleation patch of ~ 27 km between $x = 222$ km and $x = 249$ km along the fault. In the DR model, failure also occurs immediately between $x = 10$ km and $x = 75$ km, which are the regions where shallow interseismic creep is seen in the SC model (Fig. 7). This instantaneous failure does not lead to the nucleation of a large earthquake, but does emit seismic waves. The associated stress drops are on the order of ~ 0.1 MPa and thus low compared to the stress drop of the main rupture. The friction increases slightly in the velocity-strengthening sediments from its static value of 0.0176 to a dynamic value of 0.0177. Slip rates of 0.08 m/s are reached locally and accumulate 0.04 m of slip. We do not observe pronounced interaction of the instantaneously emitted waves with the down-dip nucleating spontaneous rupture event. Importantly, the DR instantaneous failure of the SC creeping sections leaves behind a heterogeneous initial stress configuration close to, but not at, failure (S parameter ~ 0.01 after the initial stress drops, see Appendix D). These fault sections are readily re-activated by the main rupture later on. Another considerable instantaneous stress drop of ~ 4.0 MPa occurs between $x = 219$ km and $x = 222$ km along the fault. Although this stress drop is also low compared to the stress drop of the main rupture, the downwards travelling emitted seismic waves do interact with the upward travelling main rupture front. However, the associated mean slip rate of 0.0022 m/s and slip of 0.05 m are low compared to the main rupture.

After the nucleation phase, the rupture mainly propagates updip. There is spontaneous rupture arrest below the downdip limit of the seismogenic zone 290–300 km along the fault. In the basalt, supershear rupture speeds of ~ 6100 m/s ($v_p = 6164$ m/s; $v_s = 3559$ m/s) are reached at the onset of rupture. These speeds are promoted by a low S parameter of 0–0.5 (e.g., Gabriel et al., 2012), which is defined as the ratio between initial strength excess and nominal stress drop (Das and Aki (1977b); Appendix D). Closely spaced secondary non-supershear rupture fronts (2) follow this main supershear rupture front. The rupture velocities change when the rupture enters the lower seismic velocity sediments (3). The main rupture front propagates updip at supershear velocities of ~ 3340 m/s ($v_p = 3350$ m/s; $v_s = 1934$ m/s), and the second rupture fronts travel at speeds of ~ 1750 m/s in the sediment close to its Rayleigh speed. The change in material, and hence seismic velocities, also results in an impedance contrast, which causes the reactivation of fault slip due to reflected seismic waves from the sediment–basalt transition (3). Rupture propagation in the sediments in the shallow part of the megathrust features small scale failure preceding the main rupture front arrival (4). These phases have slip rates of ~ 0.5 m/s and their rupture speeds are low with 1700 m/s. Their occurrence is promoted by (i) a very low strength excess of 1.0 MPa; and (ii) on-fault, dynamic stress accumulation preceding the main rupture front. These localised precursory phases do not merge into a combined rupture front but are overtaken by the faster main rupture.

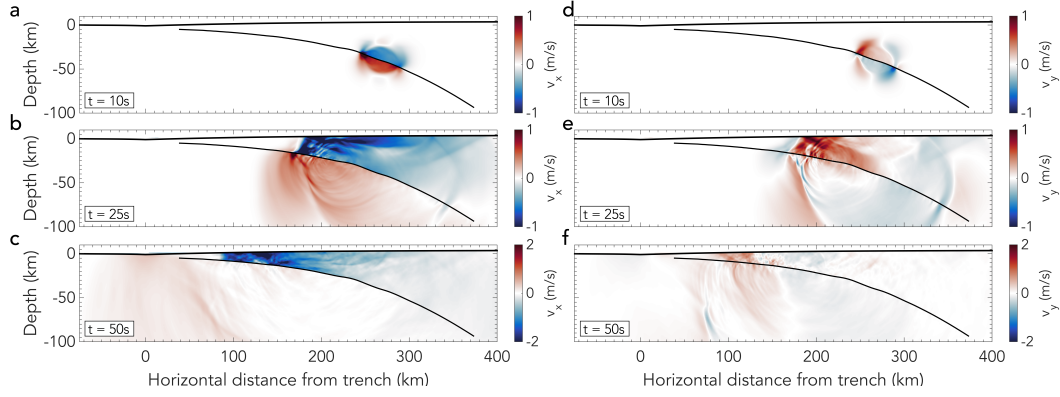


Figure 9. Horizontal (a,b,c) and vertical (d,e,f) velocity in the DR coupling model of Sec. 5.3 at $t = 10$ s, $t = 25$ s and $t = 50$ s. Fault is indicated in black.

753 The rupture is predominantly crack-like, although pulse-like behaviour is observed in the sediments. Crack-like rupture behaviour is characterised by continuous slip on the fault after arrival of the rupture front (Kostrov, 1964). During a pulse-like rupture, slip on the fault only occurs for a relatively small amount of time after the arrival of the rupture front compared to the entire duration of the rupture (Brune, 1970).
754
755
756
757
758

759 Surface reflections at (5) provide additional energy to the rupture, which results in the breaking of the shallow megathrust. This is in line with similar behaviour found by Kozdon and Dunham (2013) for dynamic rupture models of the 2011 Tōhoku-Oki earthquake. Waves are also reflected at the material contrast between sediments and basalt at (6). Later surface reflections at (7) and (8) reactivate the downdip part of the megathrust. The highest slip rate values of 10.9 m/s are reached as the rupture tip reaches the sediment-basalt transition.
760
761
762
763
764
765

766 The stress drop in Fig. 8e, calculated as the stress change with respect to the initial stress, is material dependent, with large stress drops of 14 MPa in the basalt and 5.3 MPa in the sediments. The average stress drop between the 150°C and 450° isotherms is 9.3 MPa. Initially, there is little stress drop in the velocity-strengthening region at the updip limit of the seismogenic zone. However, after ~ 70 s, the stresses drop in the sediments, even though fault slip has stopped. This could be due to (i) dynamic on-fault stress transfers caused by healing fronts of the rupture pulses (e.g., Nielsen & Madariaga, 2003; Gabriel et al., 2012), or (ii) dynamically triggered reactivation of the fault by the seismic waves (e.g., Belardinelli et al., 2003).
767
768
769
770
771
772
773
774

775 The corresponding final slip distribution in Fig. 8f shows that the maximum slip of 57.9 m (disregarding the unphysical isolated peaks) occurs in the sediments, at the frictional updip limit of the seismogenic zone. Slip tapers off towards the trench and the downdip limit of the seismogenic zone.
776
777
778

779 Fig. 9 visualises the wave field at several time steps. At 10 s the rupture just nucleates completely (also see Fig. 8d) and the wave field looks relatively simple. After 25 s, complex interactions between the free surface and the emitted waves are visible. Most notably, a large reflected wave is travelling towards the fault. After 50 s most of the waves are trapped in the accretionary wedge. This results in continuous reactivation of the fault slip which highly increases the slip in the shallow part of the fault.
780
781
782
783
784
785

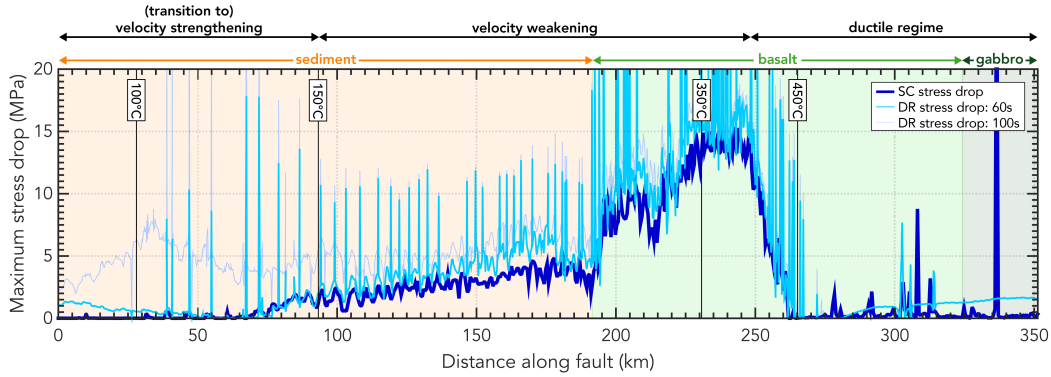


Figure 10. Maximum stress drop in the SC model and DR model (after the first 60 s and at the end of the event at 100 s) along the fault. The peaks of high stress drop in the DR model responsible for the stripes in Fig. 8e are directly related to the input from the SC model. Since the resolution in the DR model is higher, isolated fault points get affected by the interpolation of the coarser model input from the SC model. Frictional regimes dependent on temperature are indicated with corresponding isotherms (solid black lines). Background colours represent the material through which the fault is going.

786
787

5.4 Comparison of events in the seismic cycle and dynamic rupture models

788
789
790
791
792
793

Both events nucleate in the same location, which demonstrates the successful coupling of fault stress and strength conditions (Fig. 7 and 8). These coupled initial conditions then affect the full dynamic rupture behaviour. Most notably, they cause spontaneous rupture arrest at depth ($z = 65$ km) in the DR model due to the increase of strength excess when the deformation mechanism changes from brittle to ductile in the SC model (Sec. 5.1).

794
795
796
797
798
799
800
801
802
803
804

Using the stress and yield stress of the SC model as input for the DR model results in material dependent stress drop in the DR model. Prior to slip reactivation due to wave reflections, the stress drop values and distribution of the DR event are similar to those of the SC event (Fig. 10). In the nucleation region the stress drop is on the order of ~ 14 MPa. After 60 s of rupture, the stress drop in the DR model increases due to reactivation of rupture due to the reflected seismic waves that are not present in the SC model. Therefore, the DR model shows higher final stress drops in the sediments than in the SC model. The similarity of the stress drops between the models before the reactivation of fault slip in the DR model demonstrates the successful coupling of the two codes even though their friction behaviour is described by different laws (secs. 2.3 and 3.2).

805
806
807
808

The slip distribution and absolute values of the SC and DR model are different, since the DR model additionally resolves the emitted seismic waves that reactivate fault slip and uses a lower Poisson's ratio. The contributions of the reflected waves and Poisson's ratio on fault slip are explored in Secs. 5.5 and 6.1.1.

809
810
811
812

In summary, the SC and DR rupture are qualitatively comparable in terms of rupture nucleation, propagation, and arrest. They are also quantitatively comparable in terms of stress drop. However, the amount of slip is significantly larger in the DR model.

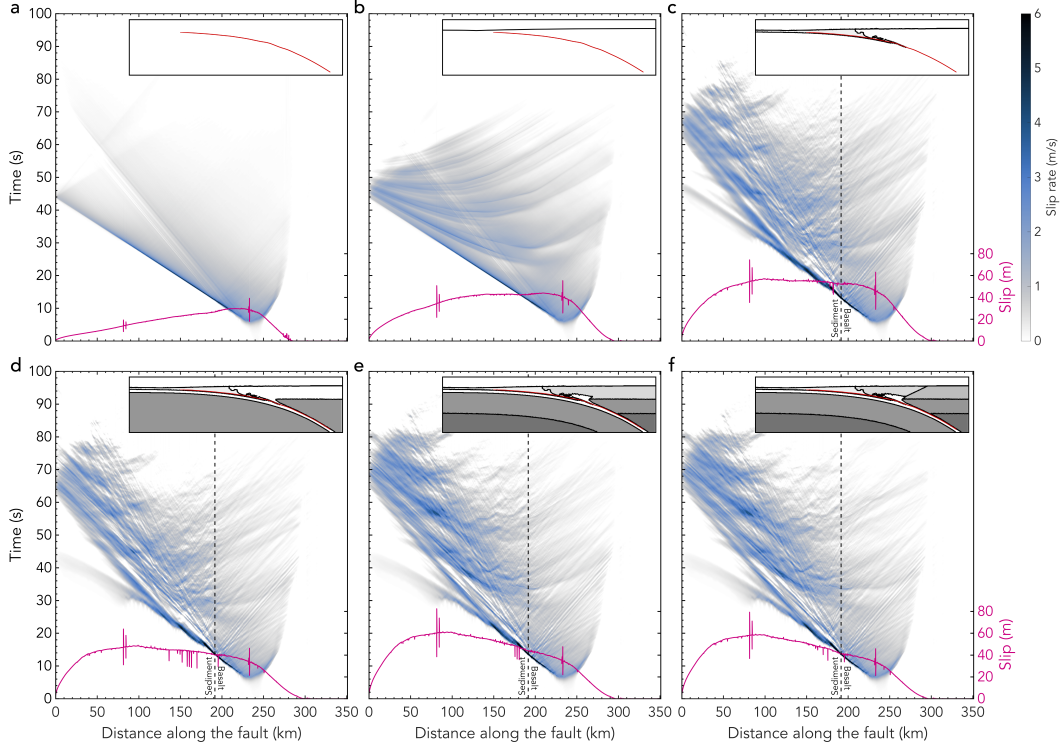


Figure 11. Slip rate evolution of a megathrust rupture for (a) a homogeneous model with basaltic composition and an extended top boundary to exclude any interactions of the seismic waves with the free surface; (b) a homogeneous model with basaltic composition including the free surface as the top boundary condition; (c) the model of Fig. 11b with the addition of incoming sediments; (d) the model of Fig. 11c with the addition of lithospheric mantle; (e) the model of Fig. 11d with the addition of asthenospheric mantle and accretionary wedge sediments; (f) the model of Fig. 11e with the addition of continental crust. Insets show the lithological structure (grey scale colours) and impedance contrasts (black) (Fig. 4a). Dotted line indicates material change between basalt and sediments. Pink lines show the final slip distribution on the fault.

813

5.5 The role of complex lithological structures

814

815

816

817

818

819

820

821

822

823

824

825

826

827

A common simplification in many dynamic rupture studies is the use of homogeneous material and friction parameters (e.g., Ma, 2012; Huang et al., 2013). However, in models that include material contrasts, particularly close to the fault, it has been shown that lithological structures affect the rupture (e.g., Huang et al., 2014; Pelties et al., 2015; Lotto et al., 2017). Lithological structures refer to large scale rock or material variations with different properties. Waves reflecting off lithological contrasts are governed by the impedance contrast between rock types. Seismic impedance Z is defined as seismic wave velocity times density ($Z = v \cdot \rho$, see Tables 2 and 3 for values). Large impedance contrasts favour wave reflection, whereas no or small impedance contrasts favour wave transmission. The reflected waves can impact the fault again which affects the on-fault stress field and thereby the rupture dynamics. For example, the resulting on-fault stress changes can lead to the (re-)activation of fault slip and alter the rupture speed (Sec. 5.3; Kozdon & Dunham, 2013; Huang et al., 2014; Pelties et al., 2015).

828 The SC model provides a complex geometry with temperature-dependent elastic
 829 properties for the DR model, which results from millions of years of thermo-
 830 mechanically coupled subduction. We systematically increase the complexity of our
 831 models from homogeneous material parameters up to the complex temperature-dependent
 832 coupling model presented in Sec. 5.3 to analyse the effect of each lithological entity
 833 on the rupture dynamics. As initial stresses, we keep the stresses that the SC model
 834 provides. This means that the stress difference between accretionary sediments and
 835 basalt is included in the initial stresses of all these models, even though the accre-
 836 tionary sediments themselves might not be included as an explicit material contrast.
 837 Here, we focus on the added effect of reflected and refracted waves from the free surface
 838 and material contrasts impacting the fault and reactivating fault slip. Compared to
 839 these effects, the stress inconsistency in the models with homogeneous material prop-
 840 erties is of secondary importance as they are not observed to significantly alter the slip
 841 rate evolution. Hence, it does not affect any of our findings presented here. Fig. 11
 842 shows the slip rate evolution for six models with an increasingly complex lithological
 843 structure as depicted by the insets. The corresponding final slip distribution is also
 844 indicated in each panel.

845 In the simplest model, we consider a homogeneous medium with basaltic material
 846 properties. We remove the free surface by extending the top boundary and placing
 847 absorbing boundary conditions on it (Fig. 11a). This effectively removes any reflections
 848 of the seismic waves from impedance contrasts or the free surface. The ensuing rupture
 849 is a supershear crack followed by a subshear crack. The crack-like nature of the rupture
 850 leads to a maximum slip accumulation in the nucleation region, which tapers towards
 851 the surface and brittle-ductile transition. The maximum slip that is reached in this
 852 homogeneous model is 29.5 m, which is twice as low as the maximum slip in the fully
 853 complex model of Sec. 5.3. The slip distribution is similar to the one from the SC
 854 model (Fig. 8c), which does not account for seismic waves. In the shallowest 100 km
 855 of the fault, the maximum slip is 16.7 m. This is more than 3 times less than in the
 856 model from Sec. 5.3, where the peak slip of 57.9 m is reached in the shallowest 100 km
 857 of the fault.

858 When a free surface is added to the model in Fig. 11a, the seismic waves reflect
 859 off of it. When they reach the fault, these reflections lower the normal stress on the
 860 fault. This results in an increase in fault slip rate and associated reactivation of fault
 861 slip (Fig. 11b). Because of the prolonged slip reactivation, the rupture duration and
 862 the total amount of slip on the fault increases. The slip is particularly increased in the
 863 shallow part of the fault where the reactivation of fault slip due to reflected waves is
 864 most pronounced.

865 When the incoming sediments of the accretionary wedge are added to the model
 866 in Fig. 11c, they introduce a low-velocity region, as the seismic velocities of the sedi-
 867 ments are lower than that of the surrounding basalt. The impedance contrast between
 868 the sediments ($Z = 8.7 \cdot 10^6 \text{ kg / s m}^2$) and basalt ($Z = 18.5 \cdot 10^6 \text{ kg / s m}^2$) is large.
 869 This addition to the model results in a change of the rupture behaviour from predom-
 870 inantly crack-like to pulse-like. Pulse-like behaviour of the rupture is promoted by
 871 reflections that induce a stress change favourable for fault slip. Whether a reflection
 872 induces a positive or negative stress change depends on their polarity. When a stress
 873 change occurs that is unfavourable for slip, the slip on the fault stops which results in
 874 pulse-like behaviour (Huang et al., 2014).

875 The large impedance contrast also causes a large portion of the seismic waves to
 876 get trapped in the incoming sediments (also see Fig. 9). This results in a complex slip
 877 reactivation pattern on the fault that increases the accumulated slip on the fault in the
 878 sediments. The isolated patches of subducted sediment in the basalt in the vicinity
 879 of the sediment-basalt transition also cause a lot of wave reflections, refractions and

880 interactions. This leads to pronounced rupture fronts in the basalt. Small nucleations
 881 in the sediments are facilitated by the low strength excess in the sediments.

882 The addition of lithospheric mantle changes the shape of the slip distribution
 883 (Fig. 11d). Waves reflecting from the free surface impact the deeper part of the fault
 884 less heavily than before, because the impedance contrast between the basaltic top
 885 layer and the lithospheric mantle is smaller and leads to less reflections. The lower
 886 wave amplitudes result in less fault slip reactivation in the basalt than in Fig. 11c.
 887 Therefore, the accumulated slip in the basaltic part of the fault is lower. The addition
 888 of lithospheric mantle also effectively transforms the deeper part of the fault that is
 889 going through the basalt into a low velocity region. However, the impedance con-
 890 trast between the lithospheric mantle and the basalt is more than twice as low as the
 891 impedance contrast between the basalt and sediments. The effect of this lower velocity
 892 region is therefore not as pronounced as in Fig. 11c and we do not see pulse-like rup-
 893 ture behaviour in the basalt. The pulse-like behaviour of the rupture in the sediments
 894 is enhanced, even though the lithospheric mantle and the incoming sediments are not
 895 directly adjacent.

896 Adding asthenospheric mantle material to the model does not change any of the
 897 on-fault properties or the rupture. This is due to the low impedance contrast between
 898 lithospheric and asthenospheric mantle. Combined with the large distance between
 899 this impedance contrast and the fault, the on-fault effect of this material contrast is
 900 negligible on the rupture dynamics.

901 The addition of the accretionary wedge sediments adds a larger impedance con-
 902 trast at the base of the wedge with the basalt (Fig. 11e). There is also an impedance
 903 contrast between the accretionary and incoming sediments, which causes additional
 904 reflections. This results in more reactivation of slip within the sediments.

905 The continental crust of the overriding plate is the last component of the SC
 906 subduction zone setup that we add to the model (Fig. 11f). Its addition results in less
 907 slip reactivation on the fault. Hence, the accumulated slip in Fig. 11f (maximum slip
 908 disregarding the unphysical slip peaks at isolated fault points is 59.2 m) is less than in
 909 Fig. 11e (maximum slip disregarding the unphysical slip peaks at isolated fault points
 910 is 61.4 m).

911 The models in Fig. 11 all assume constant material properties per rock type.
 912 However, one of the advantages of the SC model is that it provides temperature-
 913 and pressure-dependent densities. Comparing the model of Fig. 11f to Fig. 8d shows
 914 that the slip pulses on the fault are less pronounced when a temperature-dependent
 915 density is considered. This is due to less energetic reflections from decreased impedance
 916 contrasts related to the gradual increase of density and their related seismic velocities.
 917 Hence, the use of temperature-dependent properties leads to ~ 1 – 2 m less slip on the
 918 fault.

919 In summary, these results show that material contrasts influence the rupture
 920 dynamics by causing slip reactivation on the fault and influencing the final slip dis-
 921 tribution. The model with purely homogeneous material properties significantly un-
 922 derestimates the shallow fault slip by a factor 3 and results in a vastly different slip
 923 distribution. Using the temperature-dependent material contrasts of the SC model
 924 consistent with the fault geometry, stress, and yield stress, is crucial to resolve the
 925 complex wave interactions during rupture in a subduction zone which in turn affects
 926 the dynamics of the megathrust earthquake.

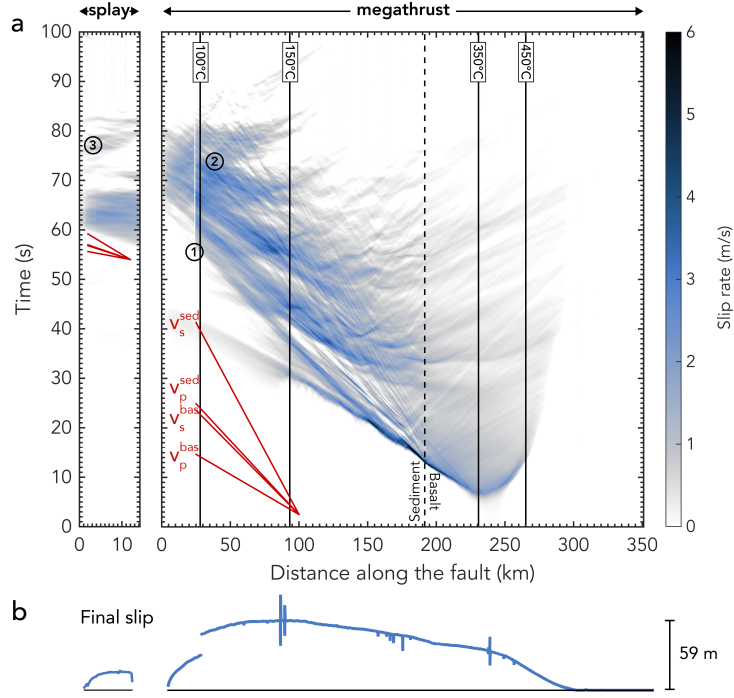


Figure 12. Slip rate evolution with time (a) and final accumulated slip (b) along the fault for both the splay fault (left column, note the horizontal exaggeration with respect to the megathrust fault x -axis) and the megathrust (right column). The splay fault connects to the megathrust at $x = 24.5$ km along the megathrust fault. Solid lines indicate the isotherms that define the frictional regimes; dashed line indicates material change. The P- and S-wave velocities v_p and v_s for both the basalt (bas) and sediment (sed) are indicated in red in both the splay and megathrust panels. Numbers are discussed in the text. The branching point on the megathrust and the two adjacent points to the left of the branching point are not plotted, as they show an unphysical numerical instability. Peak slip is indicated.

5.6 The impact of physically consistent stresses on splay fault activation

For simplicity, we only considered a rupture along the megathrust in the previous sections. However, the SC model shows high strain rate localisation along a splay fault instead of the shallow megathrust. However, the slip rates are not high enough to reach the threshold that defines a seismic event (Secs. 4.1 and 4.4). Here, we introduce the splay fault to the model by activating its internal frictional boundary condition so that slip on the splay fault is theoretically possible. This allows us to analyse if the splay fault is activated in the DR model when seismic waves are taken into account.

The resulting rupture evolution in terms of its slip rate and the final slip distribution of both the megathrust and splay fault are shown in Fig. 12. The splay fault in the DR model is activated at 56 s (Fig. 12a). Comparison with the reference model in Fig. 8 shows that both ruptures have a similar evolution. When the splay fault is activated at (1), the rupture chooses the splay fault over the megathrust and it continues at much lower slip rates on the megathrust than in the reference model (~ 56 – 68 s). This is also clearly illustrated in the final slip profile (Fig. 12b), as the final slip on the shallow megathrust is sharply reduced at the location of the splay fault compared to the reference model (Fig. 8f). Instead, we see 20 m of slip on the splay fault. When the splay fault is abandoned at approximately 68 s, the rupture in the shallow part of the megathrust looks very similar to the reference model results with the exception that small reflections from the splay fault on the megathrust are visible in the splay model (2). The last surface reflection at ~ 74 s reactivates the splay fault (3). Combining the slip on the splay fault with that of the shallowest megathrust fault, we see that the same amount of slip is accumulated in total as on the megathrust in the DR model of Sec. 5.3.

In summary, our model shows that the splay fault is indeed activated in the DR model, depicting maximum slip rates of 2.4 m/s and a maximum slip of 20 m, which is much higher than what is observed in the corresponding SC model. Therefore, we need to account for additional fault complexities such as faults splaying off from the megathrust interface to fully assess the seismic and tsunami hazard of subduction zone earthquakes.

6 Discussion

By coupling a geodynamic seismic cycle model to a dynamic rupture model, we successfully modelled the geodynamic evolution of a subduction zone down to a single dynamic earthquake rupture of the megathrust. Broad rupture characteristics, such as the rupture nucleation, propagation, and arrest, of the SC event and its corresponding DR counterpart are qualitatively comparable. The seismic waves and a complicated subsurface structure affect the slip distribution on the fault, rupture style and duration. A homogeneous model significantly underestimates shallow fault slip, which has implications for tsunami hazard assessment. With our coupling method, we can also take into account complex fault geometries including splay faults. The complex resulting dynamic rupture highlights the need for taking all scales into account when assessing the seismic and tsunamigenic hazard of megathrust earthquakes.

In the following, we discuss our two most important coupling assumptions necessary to reconcile the SC and DR method. Namely, our choice of the Poisson's ratio, and the approximation of the SC model's rate-dependent friction by linear-slip weakening in the DR model. Lastly, we discuss limitations and future developments.

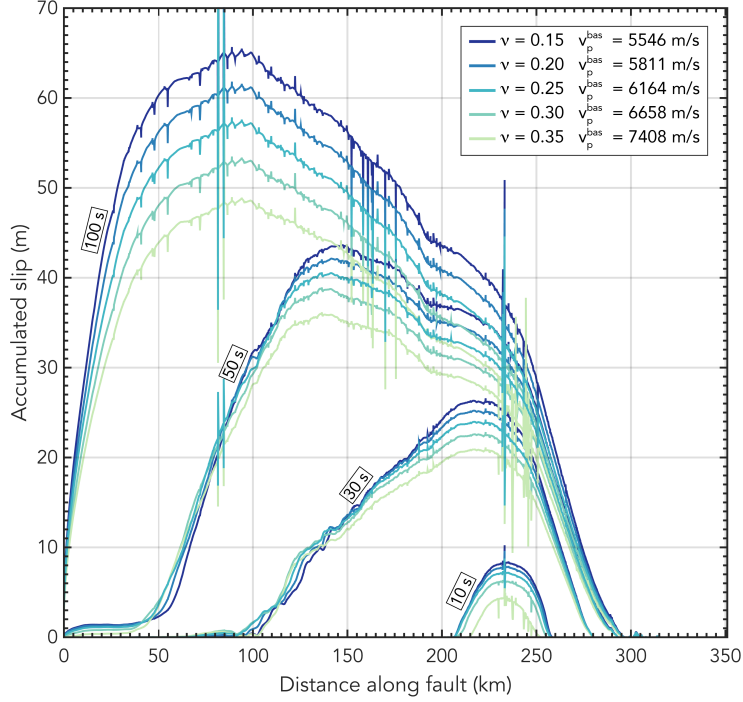


Figure 13. Accumulated slip along the fault plotted after 10 s, 30 s, 50 s and 100 s for five models where the first Lamé parameter was calculated using different Poisson’s ratios. The corresponding change in P-wave velocity is indicated for the basalt. Note that the model with $\nu = 0.25$ is the model described in Sec. 5.3.

974 6.1 Effect of coupling choices

975 6.1.1 Poisson’s ratio

976 To calculate the first Lamé parameter in the DR model from the incompressible SC model rock properties, we need to assume a Poisson’s ratio. Computational seismology often uses Poisson solids as a simplification, where $\nu = 0.25$ and therefore $\lambda_1 = G$ (e.g., Stein & Wysession, 2009; Kozdon & Dunham, 2013). In line with this, 977 978 979 we calculated λ_1 with $\nu = 0.25$ for our coupled event in Sec. 5. However, laboratory experiments indicate that there is a large variation in the Poisson’s ratio of intact rocks, e.g., the Poisson’s ratio of basalt ranges from 0.1–0.35 (Gercek, 2007). 980 981 982

983 An increase in Poisson’s ratio results in an increase of the P -wave velocity v_p , and therefore increases the difference between the P - and S -wave velocities according to 984 985

$$v_p = v_s \sqrt{\frac{2\nu}{1-2\nu} + 2}. \quad (23)$$

986 To assess this effect on our results, we run several models with different Poisson’s ratios. Models with Poisson’s ratio $\nu > 0.40$ did not result in sustained nucleation and propagation of the rupture, due to the unrealistically large seismic velocities. For 987 988 989 $\nu = 0.40$ several patches in the nucleation region are also already prohibited from rupturing. Fig. 13 shows the accumulated slip contours for several time steps for models with Poisson’s ratio 0.15 – 0.35. Larger Poisson’s ratios result in less final slip 990 991

with a maximum slip of 65.7 m for $\nu = 0.15$ and 49.0 m for $\nu = 0.35$, disregarding the unphysically high peaks in slip. This is due to a reduction in maximum slip rate and rupture duration. The latter is caused by both an increase in rupture speed and in nucleation time. The stress drop is not majorly affected by the Poisson's ratio.

Interestingly, as the slip decreases with increasing Poisson's ratio, the slip values of the DR model move towards those of the SC model, which has the highest possible Poisson's ratio of 0.5. Using a high Poisson's ratio for the model described in Fig. 11a, where seismic wave effects are non-existent would likely result in slip values similar to those of the SC model. This means that part of the slip difference between the SC and DR model can be accounted for by the difference in Poisson's ratio, while a factor of two to three of slip difference can be accounted for by fault reactivation due to wave reflections (Sec. 5.5).

The parameters affected by the Poisson's ratio (i.e., the maximum slip, rupture duration, slip rate, nucleation time, and rupture velocity) do not change the first order rupture characteristics, i.e., material dependent stress drop and predominantly updip rupture propagation, which are comparable to its SC rupture equivalent, or the rupture style.

6.1.2 Rate-dependent friction law approximation

In this study, we approximate the rate-dependent friction law of the SC model by a linear slip weakening friction law in the DR model. It is one of the simplest friction laws and it is widely used in the dynamic rupture community (e.g., Ma, 2012; Murphy et al., 2016). However, several other friction laws could have been used. For example, Olsen-Kettle et al. (2008) discusses the cubic, quintic, and septic slip weakening friction laws which are found to reduce the amount of slip.

Translating the rate-dependent friction formulation of the SC model to the linear slip weakening formulation of the DR model requires determining D_c . By ensuring both friction laws have the same strength drop with slip (Secs. 4.5 and Fig. 5), we have a physical basis for picking a certain D_c value. The resultant D_c varies between 0.7–1.1 m in the sediments, which is in line with values used in the dynamic rupture community for similar problems (e.g., Goto et al., 2012; Murphy et al., 2016). The values for D_c in the basalt are slightly higher and range from 1.0–3.5 m with values from 0.7–3.0 m in the nucleation region.

An alternative way to couple the two friction laws would be to use the characteristic slip distance corresponding to the accumulated slip at which the lowest friction value is reached in the SC model (i.e., D_c would be larger in Fig. 5). To test the effect of D_c on our model results, we run models with a constant D_c along the fault varying from 0.25–8 m. We find that the nucleation phase takes longer for increasing D_c . This is consistent with work by Bizzarri et al. (2001). With constant $D_c \geq 4$ m, we do not get nucleation at all. Besides this effect on the nucleation phase of the model, increasing D_c results in a longer rupture duration accompanied by a smaller maximum slip velocity. Stress drop, maximum slip, and rupture speed are not significantly affected. As the choice of D_c does not affect the first-order rupture characteristics, we argue that using the D_c values obtained from equating the strength drop with slip between the two models results in robust rupture dynamics.

6.2 Limitations & future work

We observe large slip in the DR model, which is inconsistent with the recurrence time reported in Sec. 4.1 for the SC model. This is due to the fact that the recurrence interval is in line with the slip in the SC model which is lower than that of the DR model. The reasons for the differences in slip between the SC and DR model are (i)

1041 the effect of seismic waves, as discussed in Sec. 5.5 and (ii) the difference in Poisson’s
 1042 ratio as discussed in Sec. 6.1.1. A future endeavour may be two-way coupling, i.e.
 1043 transferring the final stress and strain conditions from the DR model back into the SC
 1044 model, and analysing the effects on recurrence time.

1045 At present, we couple the frictional parameters of the SC model to the discrete
 1046 fault in the DR model. However, the SC model provides information on the stress field
 1047 and material strength in the entire domain. This information can be used to extend the
 1048 current DR model to account for plastic processes around the fault. Plasticity is found
 1049 to influence the overall rupture dynamics, as well as the seafloor displacements (Ma,
 1050 2012), which will crucially affect the tsunamigenic potential of the faults. The DR
 1051 model provides the ability to account for off-fault plastic deformation during coseismic
 1052 rupture (Wollherr et al., 2018) and ongoing research is concentrated on coupling the
 1053 off-fault plastic yielding of the SC model to that of the DR model (Wollherr, van Zelst,
 1054 et al., 2019).

1055 Another way to incorporate the large scale yielding in the accretionary wedge
 1056 of the SC model relies on explicitly meshing the spontaneous splay faults of the SC
 1057 model in the DR model. Besides coupling the on- and off-fault deformation between the
 1058 SC and DR model in this manner, explicitly meshing the splay faults gives additional
 1059 insight into the activation of splays in subduction zones and over several seismic cycles.
 1060 Realistically modelling splay fault activation using the constraints from the SC model
 1061 can also contribute to our understanding of tsunami generation.

1062 Currently, the here presented coupling approach is restricted to two dimensions
 1063 since the SC model is inherently two-dimensional. The extension of this coupling
 1064 approach to three dimensions is on-going work within the ASCETE (Advanced Simu-
 1065 lation of Coupled Earthquake and Tsunami Events) framework (Gabriel et al., 2018),
 1066 where the two-dimensional initial conditions from the SC model are used in the three-
 1067 dimensional version of SeisSol.

1068 By extending our approach to three dimensions (e.g., Dunham & Bhat, 2008),
 1069 accounting for off-fault plasticity (e.g., Gabriel et al., 2013), and reducing the friction
 1070 drop between static and dynamic friction, we expect that the SC initial conditions
 1071 are less favourable for supershear rupture. Changing the static friction to reduce the
 1072 supershear rupture might also be a possibility, but we refrain from doing that in this
 1073 work, because using a different friction coefficient while keeping the same stresses
 1074 would lead to an inconsistency in the coupling of the yield criterion. This would
 1075 negatively impact our achieved coupling in terms of stress drop. The high slip rate
 1076 values observed in the DR models, which are typical for purely elastic dynamic rupture
 1077 models (Andrews, 2005), may be limited by including off-fault plastic deformation.

1078 Both the SC and DR model have advantages when it comes to hazard assess-
 1079 ment. The SC model can provide insight into the recurrence interval and timing of
 1080 earthquakes, whereas the DR model can provide accurate ground motions. With our
 1081 coupled approach we combine these advantages and open new research avenues for fur-
 1082 ther methodological advances that could ultimately lead to a three-dimensional coupled
 1083 framework that includes physically consistent stress and slip for hazard assessment.

1084 7 Conclusions

1085 We couple geodynamic, seismic cycle, and dynamic rupture modelling to resolve
 1086 a wide range of time scales governing megathrust earthquake rupture. We use a
 1087 two-dimensional, visco-elasto-plastic, continuum, seismo-thermo-mechanical model to
 1088 simulate 4 Myrs of subduction dynamics and the subsequent seismic cycle. The long-
 1089 term SC model geometry features a megathrust dipping at 14° on average and a
 1090 large accretionary wedge due to sediment accretion. We model 70 quasi-periodic slip

1091 events in the seismic cycle phase, which mostly nucleate near the spontaneous down-
 1092 dip limit of the seismogenic zone. The long-term constrained state of stress varies
 1093 with lithology and reaches a maximum of 37.8 MPa just above the brittle-ductile
 1094 transition. For the coupling, we use a representative SC slip event with maximum
 1095 slip at the nucleation region near the down-dip limit of the seismogenic zone. The
 1096 ductile regime is characterised by low stresses due to viscous stress relaxation and is
 1097 accompanied by distributed ductile creep.

1098 We then couple the full complexity of spatially heterogeneous, self-consistent
 1099 fault stress and strength, material properties, and megathrust geometry at the onset
 1100 of the SC slip event to a dynamic rupture model. The use of an unstructured triangular
 1101 mesh allows for a complex megathrust geometry that results from the SC model. The
 1102 dynamic rupture model resolves spontaneous earthquake rupture jointly with seismic
 1103 waves in a two-dimensional elastic model of the megathrust interface.

1104 The SC and DR events both nucleate and arrest spontaneously at the same
 1105 locations. The stress drop in both models compares well and is material dependent,
 1106 with sediments exhibiting a stress drop of ~ 3 MPa in contrast to values of up to
 1107 10 MPa in basaltic regions.

1108 The dynamic rupture propagates primarily updip in a crack-like fashion within
 1109 the basalt and in a more pulse-like manner within the sediments. Both sections exhibit
 1110 sustained supershear rupture speeds due to a small relative strength throughout the
 1111 megathrust.

1112 We systematically demonstrate the pronounced effects of complex lithological
 1113 structures on rupture complexity, slip accumulation and dynamic fault reactivation.
 1114 Removing all impedance contrasts that reflect waves decreases peak slip by a factor
 1115 two. The homogeneous model shows a similar slip distribution to the SC model, which
 1116 also does not account for reflecting seismic waves. The inclusion of an effective low-
 1117 velocity zone in the form of sediments changes the rupture style from predominantly
 1118 crack-like to pulse-like. In addition, seismic waves get trapped in the sediment layer
 1119 which results in continuous reactivation of fault slip, particularly in the shallow part
 1120 of the fault.

1121 Within the presented coupling framework, we are able to include additional fault
 1122 structures based on strain localisation in the SC model. Adding a splay fault to the
 1123 dynamic rupture simulation results in preferred splay activation. Reflected waves also
 1124 activate the megathrust.

1125 Subduction zone geometry, lithology, fault stresses and strength, as constrained
 1126 by subduction evolution and seismic cycles, crucially affects the first-order features of
 1127 earthquake rupture dynamics. Our study also reveals important dynamic effects not
 1128 captured in seismic cycle approaches, such as the effect of seismic wave reflections from
 1129 the free surface on shallow slip accumulation in subduction zones. The SC results in
 1130 terms of stress magnitude and variability constrained by 4 Myrs of subduction can
 1131 be used as a guideline for setting up dynamic rupture models of subduction zone
 1132 megathrusts and splay faults. This study highlights the key relationships between
 1133 subduction zone processes and earthquake dynamics across temporal and spatial scales.

1134 **Appendix A Initial conditions governing the SC model**

1135 To initiate and sustain subduction, we apply a constant velocity of 7.5 cm/year
 1136 to the subducting slab (Fig. 1), which is in line with observations for Southern Chile
 1137 (Lallemand et al., 2005). Subduction initiation is further accommodated by a weak
 1138 zone (Fig. 1), which follows a wet olivine flow law and has very low plastic strength
 1139 (Table 2; Gerya & Meilick, 2011). After 3.2 million years, the initial weak zone is

1140 artificially removed and replaced with lithospheric mantle, so that the weaker material
 1141 does not influence the model any more when a suitable subduction geometry has been
 1142 obtained.

1143 The initial temperature field is calculated by considering *i*) the age of the sub-
 1144 ducting slab (40 Ma, Lallemand et al., 2005) according to the half space cooling model
 1145 (Turcotte & Schubert, 2002), *ii*) a linear temperature increase for the first 100 km of
 1146 the continental crust from 0°C to 1300°C, and *iii*) a 0.5°C km⁻¹ temperature gradient
 1147 in the asthenospheric mantle.

1148 **Appendix B Boundary conditions of the SC model**

1149 We adopt the same boundary conditions as van Dinther, Gerya, Dalguer, Mai, et
 1150 al. (2013) with free slip boundary conditions at the sides, which allow material to freely
 1151 move tangential to the boundaries, and an open boundary condition at the bottom
 1152 (Fig. 1). To enhance the decoupling of the lithosphere from the boundaries, we use
 1153 prescribed low viscosity regions at the side and bottom boundaries of the model (van
 1154 Dinther, Gerya, Dalguer, Mai, et al., 2013). We apply viscosity limits of minimum
 1155 $1 \cdot 10^{17}$ Pa s and maximum $1 \cdot 10^{25}$ Pa s throughout the model.

1156 Due to the nature of the finite difference method, we do not have a true free
 1157 surface in the SC model. Therefore, we use the sticky air method (Cramer et al.,
 1158 2012), which is a widely used proxy for a free surface in finite difference geodynamics.
 1159 The sticky air method consists of a layer of so-called ‘sticky air’ with low viscosity and
 1160 density at the top of the model where the top boundary condition is free slip (Table 2).
 1161 It allows the air-crust interface to behave as a free surface which can accommodate
 1162 topography evolution.

1163 The temperature is set to 0°C at the top of the domain and we impose zero heat
 1164 flux at the sides. At the bottom boundary, we have a constant temperature boundary
 1165 condition.

1166 **Appendix C Dominant deformation mechanism SC model at coupling** 1167 **time step**

1168 We evaluate the dominant deformation mechanism in the SC model at the cou-
 1169 pling time step by looking at the visco-elasticity factor F , which is defined as

$$F = \frac{G\Delta t}{G\Delta t + \eta_{vp}} \quad (\text{C1})$$

1170 where G is the shear modulus, Δt is the time step, and η_{vp} is the effective visco-plastic
 1171 viscosity. When there is no plastic deformation η_{vp} equals η (Eq. 8). Otherwise, when
 1172 there is plastic deformation, η_{vp} equals $\eta \cdot \frac{\sigma'_{II}}{\eta\chi + \sigma'_{II}}$, where σ'_{II} is the second invariant of
 1173 the deviatoric stress tensor and χ is the plastic multiplier. For purely elastic behaviour,
 1174 F approaches 0, while F approaches 1 for purely viscous behaviour.

1175 Fig. C1 shows the visco-elasticity factor of the SC model at the coupling time
 1176 step (Sec. 4.1). It shows that stresses in the seismogenic zone (i.e., between 150°C
 1177 and 350°C) are essentially completely elastic (i.e., $F < 0.05$). At higher temperatures
 1178 the viscous component starts to increase slowly, which results from dislocation creep
 1179 in the ductile regime. In the sticky air layer at the top of the model, the deformation
 1180 mechanism is completely viscous such that the free surface does not interfere with the
 1181 lithosphere (Cramer et al., 2012).

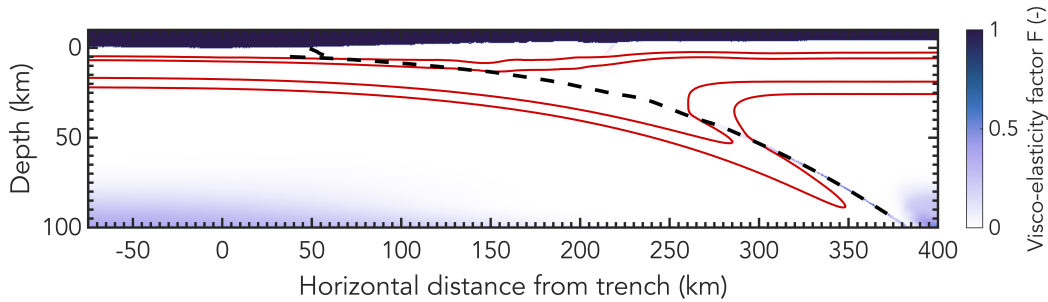


Figure C1. Visco-elasticity factor F in the SC model for the coupling time step. Faults are indicated by the dashed line. The temperature contours, which define the frictional regimes and hence seismogenic zone, are indicated in red.

1182 Appendix D Relative strength in the DR model

1183 To estimate the initial closeness to failure of the fault, we can use several different
 1184 measurements. In the geodynamics community, the strength excess is commonly used,
 1185 which is the difference between the yield strength of the rock and the initial stresses
 1186 (Fig. 7b). In the dynamic rupture community it is more common to calculate the
 1187 relative strength or so-called S parameter. We calculate the relative strength S for
 1188 the DR model according to the following formula (Das & Aki, 1977a)

$$S = \frac{\tau_s - \tau_0}{\tau_0 - \tau_d} \quad (\text{D1})$$

1189 where $\tau_s = \sigma_{\text{yield}}^{\text{dr}} = C + \mu_s \sigma_n$ is the fault yield strength or initial static strength of
 1190 the material (Sec. 3.2). $\tau_d = \sigma_{\text{sliding}}^{\text{dr}} = \sigma_n \mu_d$ is the sliding strength of the material,
 1191 which can also be called the dynamic strength of the material. τ_0 is the initial shear
 1192 stress. Note that the cohesion C does not enter the sliding strength of the fault. This
 1193 is different to the SC model, where the bulk cohesion is always present in the yield
 1194 criterion and strength of the material.

1195 Fig. D1 shows that large parts of the fault are initially at failure with $S = 0$.
 1196 However, these regions do not all result in sustained rupture, as discussed in Sec. 5.3.
 1197 After ~ 15 s, the shallow part of the fault is no longer at failure, i.e. $S > 0$, although
 1198 the relative strength is still very low, on the order of 0.05. When the main rupture
 1199 arrives in the shallow part of the fault, it breaks again and S decreases to 0. The
 1200 relative strength in the ductile regime is large ($S \gg 1$, up to 396), which prohibits
 1201 rupture on that part of the fault.

1202 A low relative strength promotes supershear pulses and cracks (e.g., Gabriel et al.,
 1203 2012), which is indeed what occurs for the sustained main rupture in the DR model
 1204 (Sec. 5.3). We note that the difference between initial loading stress and effective
 1205 peak strength of the geodynamically constrained fault is on average well comparable
 1206 to previous dynamic rupture models (e.g., Kozdon & Dunham, 2013). However, the
 1207 large strength drop to low levels of dynamic sliding resistance causes the relative overall
 1208 weakness in the DR model. The large strength drop in the DR model results from
 1209 the 70% drop in friction used in the SC model (instead of e.g., 10% in Kozdon and
 1210 Dunham (2013)) that features enhanced dynamic weakening as observed in laboratory
 1211 experiments at seismic slip rates (e.g., Di Toro et al., 2011).

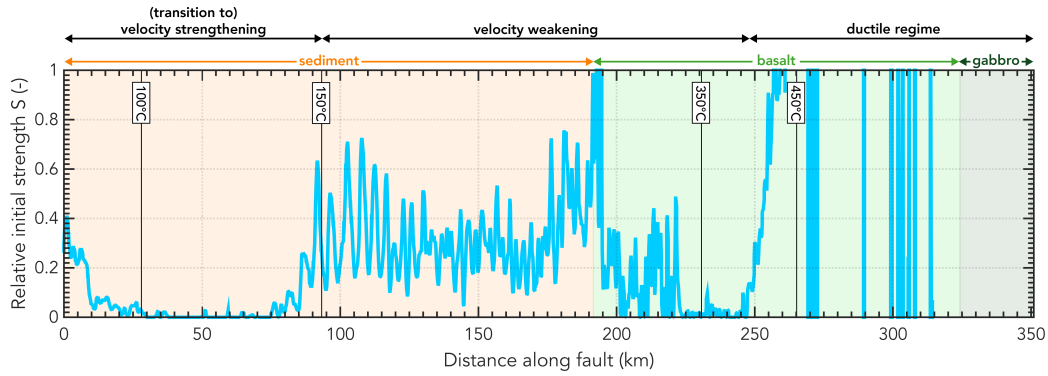


Figure D1. Relative strength S in the DR model along the fault. Frictional regimes dependent on temperature are indicated with corresponding isotherms (solid black lines). Background colours represent the material through which the fault is going.

1212 Acknowledgments

1213 We would like to thank Casper Pranger, Marie Bocher, Luca Dal Zilio, Simon
 1214 Preuss, Claudio Petrini, and Robert Herrendörfer for fruitful discussions, insights into
 1215 the SC models, and valuable comments that improved the manuscript. We would also
 1216 like to thank Carsten Uphoff for technical support relating to the meshing of the DR
 1217 model.

1218 We also thank Brad Aagaard, an anonymous reviewer, associate editor Yoshi-
 1219 hiro Kaneko, and editor Yehuda Ben-Zion for helpful comments that improved the
 1220 manuscript.

1221 Perceptually-uniform colour maps provided by Fabio Cramer and the cmocean
 1222 package by Kristen Thyng were used in this study to prevent visual distortion of the
 1223 data.

1224 Computational resources were used on the CSCS clusters Mönch and Piz Daint
 1225 (project no s741), and the ETH cluster Euler. Further computing resources were
 1226 provided by the Institute of Geophysics of LMU Munich (Oeser et al., 2006) and
 1227 the Leibniz Supercomputing Centre (LRZ, projects no h019z, pr63qo, and pr45fi on
 1228 SuperMUC).

1229 This work is part of the ASCETE project funded by the Volkswagen Foundation
 1230 (Advanced Simulation of Coupled Earthquake-Tsunami Events, grant no 88479). YvD
 1231 was funded by SNSF grants nos 200021153524 and 200021169880. SW and AAG
 1232 were funded by the European Unions Horizon 2020 research and innovation program
 1233 (ExaHyPE, grant no 671698 and ChEESE, grant no 823844), the German Research
 1234 Foundation (DFG) (projects no KA 2281/4-1, GA 2465/2-1, GA 2465/3-1), BaCaTec
 1235 (project no A4), and KONWIHR - the Bavarian Competence Network for Technical
 1236 and Scientific High Performance Computing (project: NewWave).

1237 IvZ developed the coupling method, designed the models, analysed the results,
 1238 and wrote the article. YvD and AAG initiated and contributed to the concept devel-
 1239 opment, suggested model setups, and supervised IvZ. SW and EHM contributed to
 1240 the development of the coupling method. SW also provided additional features to the
 1241 DR code specifically for the coupling method. All authors discussed the results and
 1242 contributed to the final manuscript.

1243 Input parameters for the SC model are discussed in Sec. 2.4, Appendix A and
 1244 Appendix B, and Table 2. The DR model setup is discussed in 3.3. The complete
 1245 input parameter file, megathrust and splay fault geometry, and surface geometry can
 1246 be found in the Supporting Information.

1247 References

- 1248 Aagaard, B. T., Anderson, G., & Hudnut, K. W. (2004). Dynamic rupture model-
 1249 ing of the transition from thrust to strike-slip motion in the 2002 Denali fault
 1250 earthquake, Alaska. *Bulletin of the Seismological Society of America*, *94*(6B),
 1251 S190–S201.
- 1252 Ampuero, J.-P., Vilotte, J.-P., & Sanchez-Sesma, F. (2002). Nucleation of rupture
 1253 under slip dependent friction law: simple models of fault zone. *Journal of Geo-
 1254 physical Research: Solid Earth*, *107*(B12).
- 1255 Andrews, D. (1973). A numerical study of tectonic stress release by underground ex-
 1256 plosions. *Bulletin of the Seismological Society of America*, *63*(4), 1375–1391.
- 1257 Andrews, D. (2005). Rupture dynamics with energy loss outside the slip zone. *Jour-
 1258 nal of Geophysical Research: Solid Earth*, *110*(B1).
- 1259 Angiboust, S., Wolf, S., Burov, E., Agard, P., & Yamato, P. (2012). Effect of fluid
 1260 circulation on subduction interface tectonic processes: Insights from thermo-
 1261 mechanical numerical modelling. *Earth and Planetary Science Letters*, *357*,
 1262 238–248.
- 1263 Aochi, H., & Fukuyama, E. (2002). Three-dimensional nonplanar simulation of
 1264 the 1992 Landers earthquake. *Journal of Geophysical Research: Solid Earth*,
 1265 *107*(B2), ESE–4.
- 1266 Bai, K., & Ampuero, J.-P. (2017). Effect of seismogenic depth and background
 1267 stress on physical limits of earthquake rupture across fault step overs. *Journal
 1268 of Geophysical Research: Solid Earth*, *122*(12).
- 1269 Bauer, A., Scheipl, F., Küchenhoff, H., & Gabriel, A.-A. (2017). Modeling spatio-
 1270 temporal earthquake dynamics using generalized functional additive regression.
 1271 In *Proceedings of the 32nd international workshop on statistical modelling*
 1272 (Vol. 2, pp. 146–149).
- 1273 Belardinelli, M., Bizzarri, A., & Cocco, M. (2003). Earthquake triggering by static
 1274 and dynamic stress changes. *Journal of Geophysical Research: Solid Earth*,
 1275 *108*(B3).
- 1276 Ben-Zion, Y., & Rice, J. R. (1997). Dynamic simulations of slip on a smooth fault
 1277 in an elastic solid. *Journal of Geophysical Research: Solid Earth*, *102*(B8),
 1278 17771–17784.
- 1279 Billen, M. I. (2008). Modeling the dynamics of subducting slabs. *Annual Review of
 1280 Earth and Planetary Sciences*, *36*, 325–356.
- 1281 Billen, M. I., Gurnis, M., & Simons, M. (2003). Multiscale dynamics of the Tonga-
 1282 Kermadec subduction zone. *Geophysical Journal International*, *153*(2), 359–
 1283 388.
- 1284 Bizzarri, A. (2010). How to promote earthquake ruptures: Different nucleation
 1285 strategies in a dynamic model with slip-weakening friction. *Bulletin of the
 1286 Seismological Society of America*, *100*(3), 923–940.
- 1287 Bizzarri, A., Cocco, M., Andrews, D., & Boschi, E. (2001). Solving the dynamic rup-
 1288 ture problem with different numerical approaches and constitutive laws. *Geo-
 1289 physical Journal International*, *144*(3), 656–678.
- 1290 Blanpied, M. L., Lockner, D. A., & Byerlee, J. D. (1995). Frictional slip of gran-
 1291 ite at hydrothermal conditions. *Journal of Geophysical Research: Solid Earth*,
 1292 *100*(B7), 13045–13064.
- 1293 Bormann, P., Engdahl, B., & Kind, R. (2012). Seismic wave propagation and earth
 1294 models. In P. Bormann (Ed.), *New Manual of Seismological Observatory Prac-*

- 1295 *tice 2 (NMSOP2)* (p. 1 - 105). Potsdam : Deutsches GeoForschungsZentrum
1296 GFZ.
- 1297 Brune, J. N. (1970). Tectonic stress and the spectra of seismic shear waves from
1298 earthquakes. *Journal of geophysical research*, *75*(26), 4997–5009.
- 1299 Buitter, S. J., Schreurs, G., Albertz, M., Gerya, T. V., Kaus, B., Landry, W., . . . oth-
1300 ers (2016). Benchmarking numerical models of brittle thrust wedges. *Journal*
1301 *of structural geology*, *92*, 140–177.
- 1302 Chang, C., McNeill, L. C., Moore, J. C., Lin, W., Conin, M., & Yamada, Y. (2010).
1303 In situ stress state in the Nankai accretionary wedge estimated from borehole
1304 wall failures. *Geochemistry, Geophysics, Geosystems*, *11*(12).
- 1305 Chester, F., & Higgs, N. (1992). Multimechanism friction constitutive model for
1306 ultrafine quartz gouge at hypocentral conditions. *Journal of Geophysical Re-*
1307 *search: Solid Earth*, *97*(B2), 1859–1870.
- 1308 Cisternas, M., Atwater, B. F., Torrejón, F., Sawai, Y., Machuca, G., Lagos, M., . . .
1309 others (2005). Predecessors of the giant 1960 Chile earthquake. *Nature*,
1310 *437*(7057), 404.
- 1311 Corbi, F., Funicello, F., Brizzi, S., Lallemand, S., & Rosenau, M. (2017). Control
1312 of asperities size and spacing on seismic behavior of subduction megathrusts.
1313 *Geophysical Research Letters*, *44*.
- 1314 Cramer, F., Schmeling, H., Golabek, G. J., Duretz, T., Orendt, R., Buitter, S. J. H.,
1315 . . . Tackley, P. J. (2012). A comparison of numerical surface topography cal-
1316 culations in geodynamic modelling: an evaluation of the ‘sticky air’ method.
1317 *Geophysical Journal International*, *189*(1), 38–54.
- 1318 Dalguer, L. A., & Day, S. M. (2007). Staggered-grid split-node method for spon-
1319 taneous rupture simulation. *Journal of Geophysical Research: Solid Earth*,
1320 *112*(B2).
- 1321 Dal Zilio, L., van Dinther, Y., Gerya, T. V., & Avouac, J.-P. (2019). Bimodal seis-
1322 micity in the Himalaya controlled by fault friction and geometry. *Nature com-*
1323 *munications*, *10*(1), 48.
- 1324 Dal Zilio, L., van Dinther, Y., Gerya, T. V., & Pranger, C. C. (2018). Seismic be-
1325 haviour of mountain belts controlled by plate convergence rate. *Earth and*
1326 *Planetary Science Letters*, *482*, 81–92.
- 1327 Das, S. (1980). A numerical method for determination of source time functions for
1328 general three-dimensional rupture propagation. *Geophysical Journal Interna-*
1329 *tional*, *62*(3), 591–604.
- 1330 Das, S., & Aki, K. (1977a). Fault plane with barriers: a versatile earthquake model.
1331 *Journal of geophysical research*, *82*(36), 5658–5670.
- 1332 Das, S., & Aki, K. (1977b). A numerical study of two-dimensional spontaneous
1333 rupture propagation. *Geophysical Journal of the Royal Astronomical Society*,
1334 *50*(3), 643–668.
- 1335 Day, S. M. (1982). Three-dimensional finite difference simulation of fault dynamics:
1336 rectangular faults with fixed rupture velocity. *Bulletin of the Seismological So-*
1337 *ciety of America*, *72*(3), 705–727.
- 1338 DeDontney, N., & Hubbard, J. (2012). Applying wedge theory to dynamic rupture
1339 modeling of fault junctions. *Bulletin of the Seismological Society of America*,
1340 *102*(4), 1693–1711.
- 1341 DeDontney, N., & Rice, J. R. (2012). Tsunami wave analysis and possibility of splay
1342 fault rupture during the 2004 Indian Ocean earthquake. *Pure and applied geo-*
1343 *physics*, *169*(10), 1707–1735.
- 1344 DeDontney, N., Rice, J. R., & Dmowska, R. (2012). Finite element modeling of
1345 branched ruptures including off-fault plasticity. *Bulletin of the Seismological*
1346 *Society of America*, *102*(2), 541–562.
- 1347 de la Puente, J., Ampuero, J.-P., & Käser, M. (2009). Dynamic rupture modeling on
1348 unstructured meshes using a discontinuous Galerkin method. *Journal of Geo-*
1349 *physical Research: Solid Earth*, *114*(B10).

- 1350 Del Gaudio, P., Di Toro, G., Han, R., Hirose, T., Nielsen, S., Shimamoto, T., & Cav-
1351 allo, A. (2009). Frictional melting of peridotite and seismic slip. *Journal of*
1352 *Geophysical Research: Solid Earth*, *114*(B6).
- 1353 den Hartog, S. A., Peach, C. J., de Winter, D. M., Spiers, C. J., & Shimamoto, T.
1354 (2012). Frictional properties of megathrust fault gouges at low sliding ve-
1355 locities: New data on effects of normal stress and temperature. *Journal of*
1356 *Structural Geology*, *38*, 156–171.
- 1357 Den Hartog, S. A. M., Niemeijer, A. R., & Spiers, C. J. (2012). New constraints
1358 on megathrust slip stability under subduction zone P–T conditions. *Earth and*
1359 *Planetary Science Letters*, *353*, 240–252.
- 1360 Dieterich, J. H. (1978). Time-dependent friction and the mechanics of stick-slip. In
1361 *Rock friction and earthquake prediction* (pp. 790–806). Springer.
- 1362 Dieterich, J. H. (1979). Modeling of rock friction: 1. experimental results and consti-
1363 tutive equations. *Journal of Geophysical Research: Solid Earth*, *84*(B5), 2161–
1364 2168.
- 1365 Di Toro, G., Han, R., Hirose, T., De Paola, N., Nielsen, S., Mizoguchi, K., ... Shi-
1366 mamoto, T. (2011). Fault lubrication during earthquakes. *Nature*, *471*(7339),
1367 494.
- 1368 Drucker, D. C., & Prager, W. (1952). Soil mechanics and plastic analysis or limit de-
1369 sign. *Quarterly of applied mathematics*, *10*(2), 157–165.
- 1370 Dumbser, M., & Käser, M. (2006). An arbitrary high-order discontinuous Galerkin
1371 method for elastic waves on unstructured meshes-II. The three-dimensional
1372 isotropic case. *Geophysical Journal International*, *167*(1), 319–336.
- 1373 Dunham, E. M., & Bhat, H. S. (2008). Attenuation of radiated ground motion
1374 and stresses from three-dimensional supershear ruptures. *Journal of Geophysi-
1375 cal Research: Solid Earth*, *113*(B8).
- 1376 Fujiwara, T., Kodaira, S., No, T., Kaiho, Y., Takahashi, N., & Kaneda, Y. (2011).
1377 The 2011 Tohoku-Oki earthquake: Displacement reaching the trench axis. *Sci-
1378 ence*, *334*(6060), 1240–1240.
- 1379 Fukao, Y. (1979). Tsunami earthquakes and subduction processes near deep-sea
1380 trenches. *Journal of Geophysical Research: Solid Earth*, *84*(B5), 2303–2314.
- 1381 Fulton, P., Brodsky, E. E., Kano, Y., Mori, J., Chester, F., Ishikawa, T., ... oth-
1382 ers (2013). Low coseismic friction on the Tohoku-Oki fault determined from
1383 temperature measurements. *Science*, *342*(6163), 1214–1217.
- 1384 Gabriel, A.-A., Ampuero, J.-P., Dalguer, L. A., & Mai, P. M. (2012). The transition
1385 of dynamic rupture styles in elastic media under velocity-weakening friction.
1386 *Journal of Geophysical Research: Solid Earth*, *117*(B9).
- 1387 Gabriel, A.-A., Ampuero, J.-P., Dalguer, L. A., & Mai, P. M. (2013, aug). Source
1388 Properties of Dynamic Rupture Pulses with Off-Fault Plasticity. *Journal of*
1389 *Geophysical Research: Solid Earth*, *118*(8), 4117–4126.
- 1390 Gabriel, A.-A., Behrens, J., Bader, M., van Dinther, Y., Gunawan, T., Madden,
1391 E. H., ... van Zelst, I. (2018). S21E-0492: Coupled Seismic Cycle - Earth-
1392 quake Dynamic Rupture - Tsunami Models. In *AGU Fall Meeting 2018*.
1393 Washington, D.C..
- 1394 Gabriel, A.-A., & Pelties, C. (2014). Simulating Large-Scale Earthquake Dynamic
1395 Rupture Scenarios On Natural Fault Zones Using the ADER-DG Method.
1396 In *Geophysical Research Abstracts, EGU General Assembly 2014* (Vol. 16,
1397 p. EGU2014-10572).
- 1398 Galis, M., Pelties, C., Kristek, J., Moczo, P., Ampuero, J.-P., & Mai, P. M. (2014).
1399 On the initiation of sustained slip-weakening ruptures by localized stresses.
1400 *Geophysical Journal International*, *200*(2), 890–909.
- 1401 Galvez, P., Ampuero, J.-P., Dalguer, L. A., Somala, S. N., & Nissen-Meyer, T.
1402 (2014). Dynamic earthquake rupture modelled with an unstructured 3-D spec-
1403 tral element method applied to the 2011 M 9 Tohoku earthquake. *Geophysical*
1404 *Journal International*, *198*(2), 1222–1240.

- Galvez, P., Peter, D. B., & Mai, P. M. (2018). Earthquake cycle modeling of curvilinear non-planar faults: 1992, Landers earthquake sequence. In *AGU Fall Meeting Abstracts*.
- Gercek, H. (2007). Poisson's ratio values for rocks. *International Journal of Rock Mechanics and Mining Sciences*, *44*(1), 1–13.
- Gerya, T. V. (2010). *Introduction to numerical geodynamic modelling*. Cambridge University Press.
- Gerya, T. V. (2011). Future directions in subduction modeling. *Journal of Geodynamics*, *52*(5), 344–378.
- Gerya, T. V., & Meilick, F. (2011). Geodynamic regimes of subduction under an active margin: effects of rheological weakening by fluids and melts. *Journal of Metamorphic Geology*, *29*(1), 7–31.
- Gerya, T. V., & Yuen, D. A. (2003). Characteristics-based marker-in-cell method with conservative finite-differences schemes for modeling geological flows with strongly variable transport properties. *Physics of the Earth and Planetary Interiors*, *140*(4), 293–318.
- Gerya, T. V., & Yuen, D. A. (2007). Robust characteristics method for modelling multiphase visco-elasto-plastic thermo-mechanical problems. *Physics of the Earth and Planetary Interiors*, *163*(1), 83–105.
- Geuzaine, C., & Remacle, J.-F. (2009). Gmsh: A 3-D finite element mesh generator with built-in pre-and post-processing facilities. *International journal for numerical methods in engineering*, *79*(11), 1309–1331.
- Goes, S., Agrusta, R., van Hunen, J., & Garel, F. (2017). Subduction-transition zone interaction: A review. *Geosphere*, *13*(3), 644–664.
- Goto, H., Yamamoto, Y., & Kita, S. (2012). Dynamic rupture simulation of the 2011 off the Pacific coast of Tohoku Earthquake: Multi-event generation within dozens of seconds. *Earth, planets and space*, *64*(12), 11.
- Hardebeck, J. L. (2012). Coseismic and postseismic stress rotations due to great subduction zone earthquakes. *Geophysical Research Letters*, *39*(21).
- Hardebeck, J. L. (2015). Stress orientations in subduction zones and the strength of subduction megathrust faults. *Science*, *349*(6253), 1213–1216.
- Harris, R. A. (2004). Numerical simulations of large earthquakes: Dynamic rupture propagation on heterogeneous faults. In A. Donnellan, P. Mora, M. Matsu'ura, & X.-C. Yin (Eds.), *Computational earthquake science part ii* (pp. 2171–2181). Basel: Birkhäuser Basel. doi: 10.1007/978-3-0348-7875-3_5
- Harris, R. A., Barall, M., Aagaard, B., Ma, S., Roten, D., Olsen, K., ... Dalguer, L. (2018). A suite of exercises for verifying dynamic earthquake rupture codes. *Seismological Research Letters*, *89*(3), 1146.
- Harris, R. A., Barall, M., Andrews, D., Duan, B., Ma, S., Dunham, E., ... others (2011). Verifying a computational method for predicting extreme ground motion. *Seismological Research Letters*, *82*(5), 638–644.
- Harris, R. A., Barall, M., Archuleta, R., Dunham, E., Aagaard, B., Ampuero, J., ... others (2009). The SCEC/USGS dynamic earthquake rupture code verification exercise. *Seismological Research Letters*, *80*(1), 119–126.
- Heinecke, A., Breuer, A., Rettenberger, S., Bader, M., Gabriel, A.-A., Pelties, C., ... others (2014). Petascale high order dynamic rupture earthquake simulations on heterogeneous supercomputers. In *SC14: Proceedings of the International Conference for High Performance Computing, Networking, Storage and Analysis* (pp. 3–14).
- Herrendörfer, R. (2018). *Modeling of the slip spectrum along mature and spontaneously forming faults in a visco-elasto-plastic continuum* (Unpublished doctoral dissertation). ETH Zurich.
- Herrendörfer, R., Gerya, T. V., & van Dinther, Y. (2018). An invariant rate-and state-dependent friction formulation for visco-elasto-plastic earthquake cycle simulations. *Journal of Geophysical Research: Solid Earth*.

- 1460 Herrendörfer, R., Van Dinther, Y., Gerya, T. V., & Dalguer, L. A. (2015). Earth-
 1461 quake supercycle in subduction zones controlled by the width of the seismo-
 1462 genic zone. *Nature Geoscience*, *8*(6), 471.
- 1463 Huang, Y., Ampuero, J.-P., & Helmberger, D. V. (2014). Earthquake ruptures
 1464 modulated by waves in damaged fault zones. *Journal of Geophysical Research:*
 1465 *Solid Earth*, *119*(4), 3133–3154.
- 1466 Huang, Y., Meng, L., & Ampuero, J.-P. (2013). A dynamic model of the frequency-
 1467 dependent rupture process of the 2011 Tohoku-Oki earthquake. *Earth, planets*
 1468 *and space*, *64*(12), 1.
- 1469 Ida, Y. (1973). The maximum acceleration of seismic ground motion. *Bulletin of the*
 1470 *Seismological Society of America*, *63*(3), 959–968.
- 1471 Kame, N., Rice, J. R., & Dmowska, R. (2003). Effects of prestress state and rupture
 1472 velocity on dynamic fault branching. *Journal of Geophysical Research: Solid*
 1473 *Earth*, *108*(B5).
- 1474 Kaneko, Y., Ampuero, J.-P., & Lapusta, N. (2011). Spectral-element simulations of
 1475 long-term fault slip: Effect of low-rigidity layers on earthquake-cycle dynamics.
 1476 *Journal of Geophysical Research: Solid Earth*, *116*(B10).
- 1477 Kaus, B. J. (2010). Factors that control the angle of shear bands in geodynamic nu-
 1478 merical models of brittle deformation. *Tectonophysics*, *484*(1-4), 36–47.
- 1479 Kodaira, S., Kurashimo, E., Park, J.-O., Takahashi, N., Nakanishi, A., Miura, S.,
 1480 ... Kaneda, Y. (2002). Structural factors controlling the rupture process of
 1481 a megathrust earthquake at the Nankai trough seismogenic zone. *Geophysical*
 1482 *Journal International*, *149*(3), 815–835.
- 1483 Kopf, A., & Brown, K. M. (2003). Friction experiments on saturated sediments and
 1484 their implications for the stress state of the Nankai and Barbados subduction
 1485 thrusts. *Marine Geology*, *202*(3-4), 193–210.
- 1486 Kostrov, B. V. (1964). Self similar problems of propagation of shear cracks. *Journal*
 1487 *of Applied Mathematics and Mechanics*, *28*(5), 1077–1087.
- 1488 Kozdon, J. E., & Dunham, E. M. (2013). Rupture to the trench: Dynamic rupture
 1489 simulations of the 11 March 2011 Tohoku earthquake. *Bulletin of the Seismo-*
 1490 *logical Society of America*, *103*(2B), 1275–1289.
- 1491 Kozdon, J. E., Dunham, E. M., & Nordström, J. (2013). Simulation of dynamic
 1492 earthquake ruptures in complex geometries using high-order finite difference
 1493 methods. *Journal of Scientific Computing*, *55*(1), 92–124.
- 1494 Lallemand, S., Heuret, A., & Boutelier, D. (2005). On the relationships between
 1495 slab dip, back-arc stress, upper plate absolute motion, and crustal nature in
 1496 subduction zones. *Geochemistry, Geophysics, Geosystems*, *6*(9).
- 1497 Langer, S., Olsen-Kettle, L. M., Weatherley, D., Gross, L., & Mühlhaus, H.-B.
 1498 (2010). Numerical studies of quasi-static tectonic loading and dynamic rup-
 1499 ture of bi-material interfaces. *Concurrency and Computation: Practice and*
 1500 *Experience*, *22*(12), 1684–1702.
- 1501 Lapusta, N., Rice, J. R., Ben-Zion, Y., & Zheng, G. (2000). Elastodynamic analysis
 1502 for slow tectonic loading with spontaneous rupture episodes on faults with
 1503 rate-and state-dependent friction. *Journal of Geophysical Research: Solid*
 1504 *Earth*, *105*(B10), 23765–23789.
- 1505 Lay, T., Ammon, C. J., Kanamori, H., Xue, L., & Kim, M. J. (2011). Possible
 1506 large near-trench slip during the 2011 Mw 9.0 off the Pacific coast of Tohoku
 1507 Earthquake. *Earth, planets and space*, *63*(7), 32.
- 1508 Li, S., Moreno, M., Rosenau, M., Melnick, D., & Oncken, O. (2014). Splay fault
 1509 triggering by great subduction earthquakes inferred from finite element models.
 1510 *Geophysical Research Letters*, *41*(2), 385–391.
- 1511 Liu, Y., & Rice, J. R. (2007). Spontaneous and triggered aseismic deformation
 1512 transients in a subduction fault model. *Journal of Geophysical Research: Solid*
 1513 *Earth*, *112*(B9).
- 1514 Lotto, G. C., Dunham, E. M., Jeppson, T. N., & Tobin, H. J. (2017). The effect

- 1515 of compliant prisms on subduction zone earthquakes and tsunamis. *Earth and*
 1516 *Planetary Science Letters*, 458, 213–222.
- 1517 Ma, S. (2012). A self-consistent mechanism for slow dynamic deformation and
 1518 tsunami generation for earthquakes in the shallow subduction zone. *Geophysical*
 1519 *Research Letters*, 39(11).
- 1520 Madariaga, R., Olsen, K., & Archuleta, R. (1998). Modeling dynamic rupture in
 1521 a 3D earthquake fault model. *Bulletin of the Seismological Society of America*,
 1522 88(5), 1182–1197.
- 1523 Madden, E. H., Ulrich, T., Gabriel, A.-A., van Zelst, I., & van Dinther, Y. (2017).
 1524 The role of splay faults in seafloor deformation and tsunami generation dur-
 1525 ing the Mw 9.1-9.3 Sumatra-Andaman Earthquake. In E. E. Gdoutos (Ed.),
 1526 *Proceedings of the 14th international conference on fracture*.
- 1527 Madden, E. H., Ulrich, T., Rannabauer, L., Vater, S., Gabriel, A.-A., Behrens, J.,
 1528 ... van Zelst, I. (2018). Physics-based Coupled Models of the 2018 Sulawesi
 1529 Earthquake and Tsunami. In *AGU Fall Meeting Abstracts*.
- 1530 Moresi, L., Dufour, F., & Mühlhaus, H.-B. (2003). A Lagrangian integration point
 1531 finite element method for large deformation modeling of viscoelastic geomateri-
 1532 als. *Journal of computational physics*, 184(2), 476–497.
- 1533 Murphy, S., Scala, A., Herrero, A., Lorito, S., Festa, G., Trasatti, E., ... Nielsen, S.
 1534 (2016). Shallow slip amplification and enhanced tsunami hazard unravelled by
 1535 dynamic simulations of mega-thrust earthquakes. *Scientific reports*, 6, 35007.
- 1536 Nielsen, S., & Madariaga, R. (2003). On the self-healing fracture mode. *Bulletin of*
 1537 *the Seismological Society of America*, 93(6), 2375–2388.
- 1538 Oeser, J., Bunge, H.-P., & Mohr, M. (2006). Cluster design in the earth sciences:
 1539 Tethys. In *International conference on high performance computing and com-*
 1540 *munications* (pp. 31–40).
- 1541 Oglesby, D. D., Archuleta, R. J., & Nielsen, S. B. (1998). Earthquakes on dipping
 1542 faults: the effects of broken symmetry. *Science*, 280(5366), 1055–1059.
- 1543 Olsen-Kettle, L., Weatherley, D., Saez, E., Gross, L., Mühlhaus, H.-B., & Xing, H.
 1544 (2008). Analysis of slip-weakening frictional laws with static restrengthen-
 1545 ing and their implications on the scaling, asymmetry, and mode of dynamic
 1546 rupture on homogeneous and bimaterial interfaces. *Journal of Geophysical*
 1547 *Research: Solid Earth*, 113(B8).
- 1548 Patočka, V., Čadek, O., Tackley, P. J., & Čížková, H. (2017). Stress memory ef-
 1549 fect in viscoelastic stagnant lid convection. *Geophysical Journal International*,
 1550 209(3), 1462–1475.
- 1551 Pelties, C., Gabriel, A.-A., & Ampuero, J.-P. (2014). Verification of an ADER-DG
 1552 method for complex dynamic rupture problems. *Geoscientific Model Develop-*
 1553 *ment*, 7(3), 847–866.
- 1554 Pelties, C., Huang, Y., & Ampuero, J.-P. (2015). Pulse-like rupture induced by
 1555 three-dimensional fault zone flower structures. *Pure and Applied Geophysics*,
 1556 172(5), 1229–1241.
- 1557 Pelties, C., Puente, J., Ampuero, J.-P., Brietzke, G. B., & Käser, M. (2012). Three-
 1558 dimensional dynamic rupture simulation with a high-order discontinuous
 1559 Galerkin method on unstructured tetrahedral meshes. *Journal of Geophysical*
 1560 *Research: Solid Earth*, 117(B2).
- 1561 Petrini, C., Gerya, T. V., van Dinther, Y., Connolly, J. A., & Madonna, C. (2017).
 1562 Modelling earthquakes using a poro-elastic two-phase flow formulation. In
 1563 *AGU Fall Meeting Abstracts*.
- 1564 Pollard, D., Pollard, D. D., Fletcher, R. C., & Fletcher, R. C. (2005). *Fundamentals*
 1565 *of structural geology*. Cambridge University Press.
- 1566 Preuss, S., Herrendrfer, R., Gerya, T. V., Ampuero, J.-P., & van Dinther, Y. (2019,
 1567 Jan). *Seismic and aseismic fault growth lead to different fault orientations*.
 1568 EarthArXiv.
- 1569 Ranalli, G. (1995). *Rheology of the earth*. Springer Science & Business Media.

- 1570 Rice, J. R. (1993). Spatio-temporal complexity of slip on a fault. *Journal of Geo-*
 1571 *physical Research: Solid Earth*, 98(B6), 9885–9907.
- 1572 Romanet, P., Bhat, H. S., Jolivet, R., & Madariaga, R. (2018). Fast and slow slip
 1573 events emerge due to fault geometrical complexity. *Geophysical Research Let-*
 1574 *ters*, 45(10), 4809–4819.
- 1575 Ruina, A. (1983). Slip instability and state variable friction laws. *Journal of Geo-*
 1576 *physical Research: Solid Earth*, 88(B12), 10359–10370.
- 1577 Schultz, R. (1995). Limits on strength and deformation properties of jointed basaltic
 1578 rock masses. *Rock Mechanics and Rock Engineering*, 28(1), 1–15.
- 1579 Seno, T. (2009). Determination of the pore fluid pressure ratio at seismogenic
 1580 megathrusts in subduction zones: Implications for strength of asperities and
 1581 Andean-type mountain building. *Journal of Geophysical Research: Solid Earth*,
 1582 114(B5).
- 1583 Sobolev, S. V., & Muldashev, I. A. (2017). Modeling seismic cycles of great megath-
- 1584 rust earthquakes across the scales with focus at postseismic phase. *Geochem-*
 1585 *istry, Geophysics, Geosystems*, 18(12), 4387–4408.
- 1586 Stein, S., & Wysession, M. (2009). *An introduction to seismology, earthquakes, and*
 1587 *earth structure*. John Wiley & Sons.
- 1588 Tamura, S., & Ide, S. (2011). Numerical study of splay faults in subduction zones:
 1589 The effects of bimaterial interface and free surface. *Journal of Geophysical Re-*
 1590 *search: Solid Earth*, 116(B10).
- 1591 Tsutsumi, A., & Shimamoto, T. (1997). High-velocity frictional properties of gabbro.
 1592 *Geophysical Research Letters*, 24(6), 699–702.
- 1593 Turcotte, D., & Schubert, G. (2002). *Geodynamics*. Cambridge University Press.
- 1594 Ujiie, K., Tanaka, H., Saito, T., Tsutsumi, A., Mori, J. J., Kameda, J., ... Scien-
- 1595 tists, T. (2013). Low Coseismic Shear Stress on the Tohoku-Oki Megathrust
 1596 Determined from Laboratory Experiments. *Science*, 342(6163), 1211–1214.
 1597 doi: 10.1126/science.1243485
- 1598 Ulrich, T., Gabriel, A.-A., Ampuero, J.-P., & Xu, W. (2018, Jul). *Dynamic viability*
 1599 *of the 2016 Mw 7.8 Kaikura earthquake cascade on weak crustal faults*. Earth-
 1600 ArXiv.
- 1601 Uphoff, C., Rettenberger, S., Bader, M., Madden, E. H., Ulrich, T., Wollherr, S., &
 1602 Gabriel, A.-A. (2017). Extreme scale multi-physics simulations of the tsunami-
 1603 genic 2004 sumatra megathrust earthquake. In *Proceedings of the international*
 1604 *conference for high performance computing, networking, storage and analysis*
 1605 (p. 21).
- 1606 van Dinther, Y., Gerya, T. V., Dalguer, L. A., Corbi, F., Funicello, F., & Mai,
 1607 P. M. (2013). The seismic cycle at subduction thrusts: 2. Dynamic implica-
 1608 tions of geodynamic simulations validated with laboratory models. *Journal of*
 1609 *Geophysical Research: Solid Earth*, 118(4), 1502–1525.
- 1610 van Dinther, Y., Gerya, T. V., Dalguer, L. A., Mai, P. M., Morra, G., & Giardini,
 1611 D. (2013). The seismic cycle at subduction thrusts: Insights from seismo-
 1612 thermo-mechanical models. *Journal of Geophysical Research: Solid Earth*,
 1613 118(12), 6183–6202.
- 1614 van Dinther, Y., Mai, P. M., Dalguer, L. A., & Gerya, T. V. (2014). Modeling the
 1615 seismic cycle in subduction zones: The role and spatiotemporal occurrence of
 1616 off-megathrust earthquakes. *Geophysical Research Letters*, 41(4), 1194–1201.
- 1617 Wang, K., & Hu, Y. (2006). Accretionary prisms in subduction earthquake cycles:
 1618 The theory of dynamic Coulomb wedge. *Journal of Geophysical Research:*
 1619 *Solid Earth*, 111(B6).
- 1620 Wendt, J., Oglesby, D. D., & Geist, E. L. (2009). Tsunamis and splay fault dynam-
 1621 ics. *Geophysical Research Letters*, 36(15).
- 1622 Wollherr, S., Gabriel, A.-A., & Mai, P. M. (2019). Landers 1992 “reloaded”: In-
 1623 tegrative dynamic earthquake rupture modeling. *Journal of Geophysical Re-*
 1624 *search: Solid Earth*.

- 1625 Wollherr, S., Gabriel, A.-A., & Uphoff, C. (2018). Off-fault plasticity in three-
1626 dimensional dynamic rupture simulations using a modal Discontinuous
1627 Galerkin method on unstructured meshes: Implementation, verification,
1628 and application. *Geophysical Journal International*, *214*, 1556–1584. doi:
1629 <https://doi.org/10.1093/gji/ggy213>
- 1630 Wollherr, S., van Zelst, I., Gabriel, A.-A., Madden, E. H., & van Dinther, Y. (2019).
1631 Plastic deformation and seafloor uplift in geomechanically constrained dynamic
1632 rupture models of subduction zone earthquakes. In *EGU General Assembly*
1633 *Abstracts*.